Cell Reports

Article

The adaptor protein SKT interacts with PSD-95 and SHANK3 and affects synaptic functions

Graphical abstract

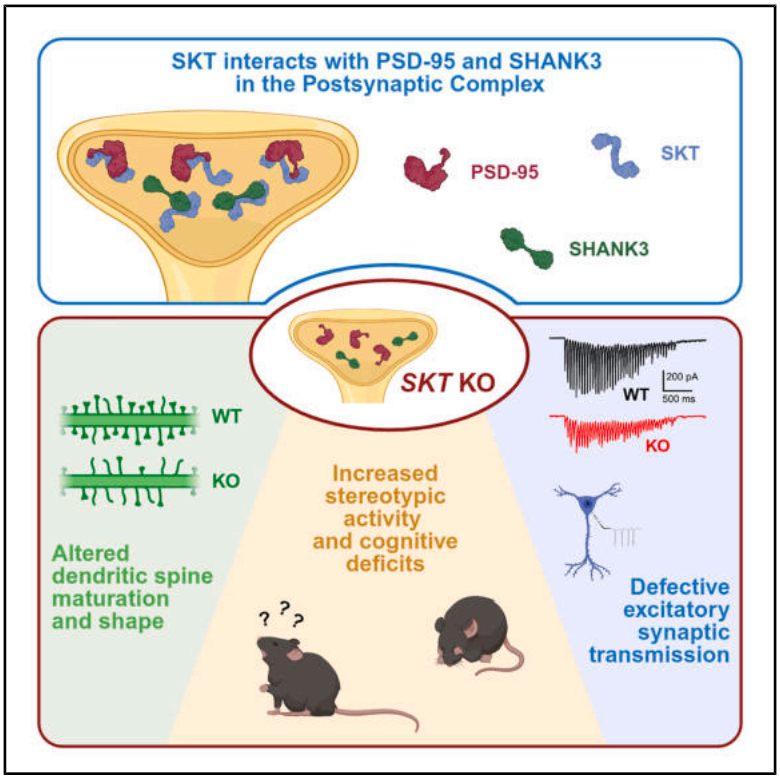

Authors

Alessandro Morellato, Mario De Gregorio, Costanza Angelini, ..., Emilia Turco, Ilaria Bertocchi, Paola Defilippi

Correspondence

ilaria.bertocchi@unito.it (I.B.), paola.defilippi@unito.it (P.D.)

In brief

Morellato, De Gregorio, Angelini, et al. identify the postsynaptic scaffold SKT as an emerging member of the postsynaptic molecular complexes. *SKT* deletion causes dendritic spine defects associated with electrophysiological abnormalities, stereotypic behavior, and motor and cognitive deficits. These data highlight the crucial role of SKT in synapse maturation and function.

Highlights

- SKT is a postsynaptic scaffold interacting directly with PSD95 and SHANK3
- *SKT* loss causes defects in dendritic spine formation, morphology, and maturation
- *SKT* loss leads to a significant reduction in excitatory synaptic transmission
- *SKT*-KO mice exhibit impaired motor, cognitive, and executive functions

Morellato et al., 2025, Cell Reports *44*, 116206
September 23, 2025
https://doi.org/10.1016/j.celrep.2025.116206

CellPress

Cell Reports

CellPress
OPEN ACCESS

Article

The adaptor protein SKT interacts with PSD-95 and SHANK3 and affects synaptic functions

Alessandro Morellato,[1,9] Mario De Gregorio,[1,9] Costanza Angelini,[1,9] Federico Torelli,[2,3] Vittorio Belmonte,[1] Annalisa Alfieri,[1] Beatrice Bersia,[1] Tiziana Cravero,[1] Marta Gai,[1] Olga Teresa Bianciotto,[1] Rebecca Oddone,[1] Vincenzo Salemme,[1] Dora Natalini,[1] Giorgia Centonze,[1] Francesca Nigrelli,[1] Alessandra Raspanti,[4] Antonia Gurgone,[4] Giacomo D'Attanasio,[1] Paolo Mele,[4,5] Carola Eva,[4,5,10] Alessandra Lodi,[4,5] Daniela Gavello,[6] Valentina Carabelli,[6] Enis Hidisoglu,[6,7] Giuseppe Chiantia,[6] Emilio Carbone,[6] Andrea Becchetti,[8] Maurizio Giustetto,[4] Andrea Marcantoni,[6] Emilia Turco,[1] Ilaria Bertocchi,[4,5,*] and Paola Defilippi[1,11,*]

[1]Department of Molecular Biotechnology and Health Sciences, University of Torino, Via Nizza 52, 10126 Torino, Italy
[2]Institute for Physiology I, University of Freiburg, Medical Faculty, 79104 Freiburg, Germany
[3]University of Freiburg, Faculty of Biology, 79104 Freiburg, Germany
[4]Department of Neuroscience "Rita Levi Montalcini," University of Torino, Via Cherasco 15, 10126 Torino, Italy
[5]Neuroscience Institute Cavalieri Ottolenghi (NICO), University of Torino, Regione Gonzole 10, 10043 Orbassano, Torino, Italy
[6]Department of Drug Science, Laboratory of Cellular and Molecular Neuroscience, University of Torino, 10126 Torino, Italy
[7]Department of Biophysics, Faculty of Medicine, Izmir Bakircay University, Izmir, Turkey
[8]Department of Biotechnology and Biosciences, University of Milano-Bicocca, Piazza della Scienza 2, 20126 Milano, Italy
[9]These authors contributed equally
[10]Deceased
[11]Lead contact
*Correspondence: ilaria.bertocchi@unito.it (I.B.), paola.defilippi@unito.it (P.D.)
https://doi.org/10.1016/j.celrep.2025.116206

SUMMARY

Postsynaptic density (PSD) is a tightly interconnected protein network ensuring synaptic function through the interaction of neurotransmitter receptors, structural adaptor proteins, and signaling molecules. Disruption of PSD may cause neurological diseases, including autism spectrum disorders and cognitive impairment. We demonstrate that the SKT adaptor distinctly localizes within dendritic spines as an integral component of the synaptic network, binding PSD-95 and SHANK3. *SKT*-knockout (KO) mice show significant abnormalities in dendritic spine density and morphology, consistent with RhoA and Rac1 GTPase dysregulated activity. KO-derived neuronal cultures display delayed neuronal synchronization and maturation associated with glutamatergic pre- and postsynaptic impairment. Behavioral tests on KO mice reveal increased self-grooming activity and impaired motor coordination, with altered cognitive and executive functions compared to wild-type mice. Overall, SKT emerges as a key contributor to the structural and functional PSD organization, regulating synaptic function through its interactions with PSD components.

INTRODUCTION

In the central nervous system, synapses enable neuron communication through synaptic regions, where the axon interacts with dendritic spines (DSs).[1] DSs are specialized bulbous protrusions extending from the dendritic shaft displaying various morphologies, from immature, elongated filopodial-shaped to mature, mushroom-shaped spines with enlarged heads. Alterations in their number and morphology are a hallmark of several neurological disorders, collectively referred to as synaptopathies.[2,3]

The synapse proteome comprises thousands of proteins assembled into multimolecular complexes.[4–6] DSs include a well-organized postsynaptic density (PSD), crucial for synaptic function, that encompasses membrane-tethered receptors and channels, cytoskeletal and cell adhesion proteins, and signaling molecules interacting with adaptor proteins to build large complexes. Alteration of a single one of these components disrupts synaptic DS morphology and function.[7]

PSD-95 is a prominent member of the membrane-associated guanylate kinase (MAGUK) family with a key role in organizing PSD complexes at the cell membrane for synaptic signaling.[8] The postsynaptic scaffold SHANK1–3 (SH3 and multiple ANKYRIN repeat domains) is distally within the PSD, extending away from the postsynaptic membrane. Alterations in these proteins have been linked to neurodevelopmental disorders, like autism spectrum disorder (ASD) and intellectual disability.[4,9] The comprehension of the composition of the PSD is still growing, with new adaptors under characterization, i.e., p140Cap and POSH.[10–13] However, the relevance of many putative PSD components, mainly identified by proteomics,[14] is still unknown. Among these, we dissect the SKT protein (with the human homolog KIAA1217), identified in the p140Cap synaptic interactome[11] and in the human postsynaptic neocortical proteome.[4,14] The

name Small with Kinky Tail derives from a large-scale gene-trap GT mutagenesis, in which *SKT*(Gt) mice exhibit abnormal intervertebral disks, leading to a specific sickle-tail phenotype.[15,16] So far, *SKT/KIAA1217* have been reported as regulators of intervertebral disk development[16] and have been implicated in lumbar disk herniation[15] and vertebral malformation.[17] The role of SKT in the brain is completely unknown, although genome-wide association studies identified *KIAA1217* as the best single gene hit for the digit span backward test used in clinical neuropsychology to assess working memory abilities.[18,19] Here, we characterize SKT as a relevant adaptor within the PSD, demonstrating its interaction with PSD-95 and SHANK3. *SKT*-knockout (KO) mice elucidate SKT modulation of synaptic plasticity, electrophysiological properties, and behavior.

RESULTS

The SKT protein is expressed in the postsynaptic compartment

SKT clusters in a small family with p140Cap, being 60% homologous with a mean 37% identity at the amino acid (aa) level, with several common domains involved in protein-protein interactions,[18] as shown in Figure 1A. Moreover, SKT shows intrinsically disordered regions (DEPICTER [Disordered Prediction Center]).[19] A specific homemade rabbit polyclonal antibody against SKT was generated (see STAR Methods and Figures S1A and S1B), showing that SKT is expressed in the brain (Figure S1B, left) with a doublet of 177 and 148 kDa bands, *bona fide* representing two different isoforms rising from alternative splicing (https://www.ensembl.org/Mus_musculus/Gene/Summary?db=core;g=ENSMUSG00000036617;r=2:19914591-20815524) (Figure S1C). Brain extracts isolated at different postnatal days (PND) show that SKT was almost undetectable at 0 PND, increased in the early phases of brain development, at 7 PND, and persisted in the adult stage (60 PND) at almost the same level (Figure 1B). SKT is well expressed in the anterior and posterior cortex and, to a lesser extent, in the other brain regions (Figure 1C). Primary astrocytes did not show detectable SKT expression (Figure S2A), suggesting that SKT is mainly expressed in the neuronal compartment and not in glial cells. By extensive synaptosome fractionation (see STAR Methods and Figure 1D), SKT was present both in the P2 and in the postsynaptic Triton-insoluble fraction (TIF) identified by high levels of PSD-95. On the contrary, SKT was almost undetectable in the P4 and in the presynaptic Triton-soluble fraction, identified by the absence of PSD-95 (Figure 1E). Confocal immunofluorescence on primary neurons at DIV 18 (days *in vitro*) shows the presence of SKT on small structures similar to DSs along the dendritic arborization (Figure 1F). Around half of SKT-positive puncta localized with PSD-95 (Figure 1G, left), and around 20% of PSD-95 spots localized with SKT (Figure 1G, right). Overall, the enrichment in TIF and the colocalization with PSD-95 indicate that SKT is present in the postsynaptic compartment of the excitatory synapses. However, staining DIV 18 primary neurons for SKT and vGAT (marker of inhibitory synapses) (Figure S2C) disclosed the apposition of SKT and vGAT at inhibitory synapses, shown by several merged white puncta localized along dendritic shafts, suggesting that SKT is likely to also regulate inhibitory synapses.

SKT interacts with PSD-95 and SHANK3

By immunoprecipitating SKT from wild-type (WT) and KO synaptosomes, we found that SKT associates with PSD-95, the SHANK family members, CAMKII-α, p140Cap, HOMER1a, and BETA-CATENIN, but not AXIN (Figure 2A), suggesting that SKT could participate in several postsynaptic macromolecular complexes.[9]

To investigate whether SKT directly interacts with the above-mentioned proteins, human embryonic kidney HEK293T cells, which do not express endogenous SKT or PSD-95 (Figure S2B), were transfected with green fluorescent protein GFP-SKT-FL (full length) along with HA-SHANK1, HA-SHANK2, or Myc-SHANK3. By coimmunoprecipitation with anti-GFP antibody, SKT was found mainly associated with SHANK3 and less with SHANK1 and SHANK2 (Figure 2B). Moreover, upon HEK293T transfection with red fluorescent protein RFP-SKT-FL along with GFP-tagged CAMKII-alpha, CAMKII-beta, HOMER1a, p140Cap, and PSD-95, SKT was found associated only with p140Cap and PSD-95 (Figure 2C) and not with CAMKII-alpha, CAMKII-beta, or HOMER1a.

PSD-95 contains three N-terminal PDZ modules that play a critical role in synapse organization, interacting with receptors, ion channels, and enzymes.[20] We generated two GFP-tagged constructs coding respectively: (1) the amino-terminal region 1–397 containing the PDZ domains or (2) the carboxy-terminal region 430–724, which includes the SH3 and GK domains[21] (Figure 2D). When HEK293T cells were transfected with RFP-SKT-FL along with GFP-PSD-95-FL or the two specific constructs, SKT interacted with PSD-95-FL and its amino-terminal 1–397 region to similar extents and not with the carboxy-terminal 430–724 region (Figure 2E). After cotransfection of RFP-SKT-FL along with the three PSD-95 constructs into COS-7 cells not expressing SKT (Figure S2B), immunofluorescence analysis showed a significantly higher localization between RFP-SKT-FL and GFP-PSD-95-FL or its amino-terminal (1–397) in comparison with the carboxy-terminal domain (430–724) (Figures 2F and 2G).

In the BioID assay, the biotin ligase BirA enzyme can biotinylate proteins in the range of 30 nm,[22] leading to the identification of proximal directly interacting proteins. We transfected HEK293T cells with either Myc-BirA-SKT (with the BirA enzyme located at the amino terminus of SKT) or SKT-BirA-HA (with the BirA enzyme located at the carboxy terminus of SKT) (Figure 3A), together with PSD-95 or SHANK3 plasmids. Both PSD-95 and SHANK3 were highly biotinylated in the presence of Myc-BirA-SKT (Figure 3B), while they were not biotinylated by SKT-BirA-HA (Figure 3C), indicating that they proximally interact with SKT, preferentially associating through the SKT amino-terminal region. p140Cap was biotinylated to similar extents by Myc-BirA-SKT and SKT-BirA-HA, indicating that both constructs were functional (Figures S3A and S3B, left). As a negative control, GFP empty vector was not biotinylated (Figures S3A and S3B, right). We then transfected HEK293T cells with either PSD-95 or SHANK3 along with the GFP-SKT-FL or the two SKT constructs, respectively encoding the amino-terminal half (1–823) and the carboxy-terminal half (824–1,943) of SKT (Figure 3D). PSD-95 (Figure 3E) and SHANK3 (Figure 3F) interacted only with GFP-SKT-FL and the amino-terminal region 1–823, confirming the biotinylation results. We also analyzed the localization in COS-7 cells upon transfection

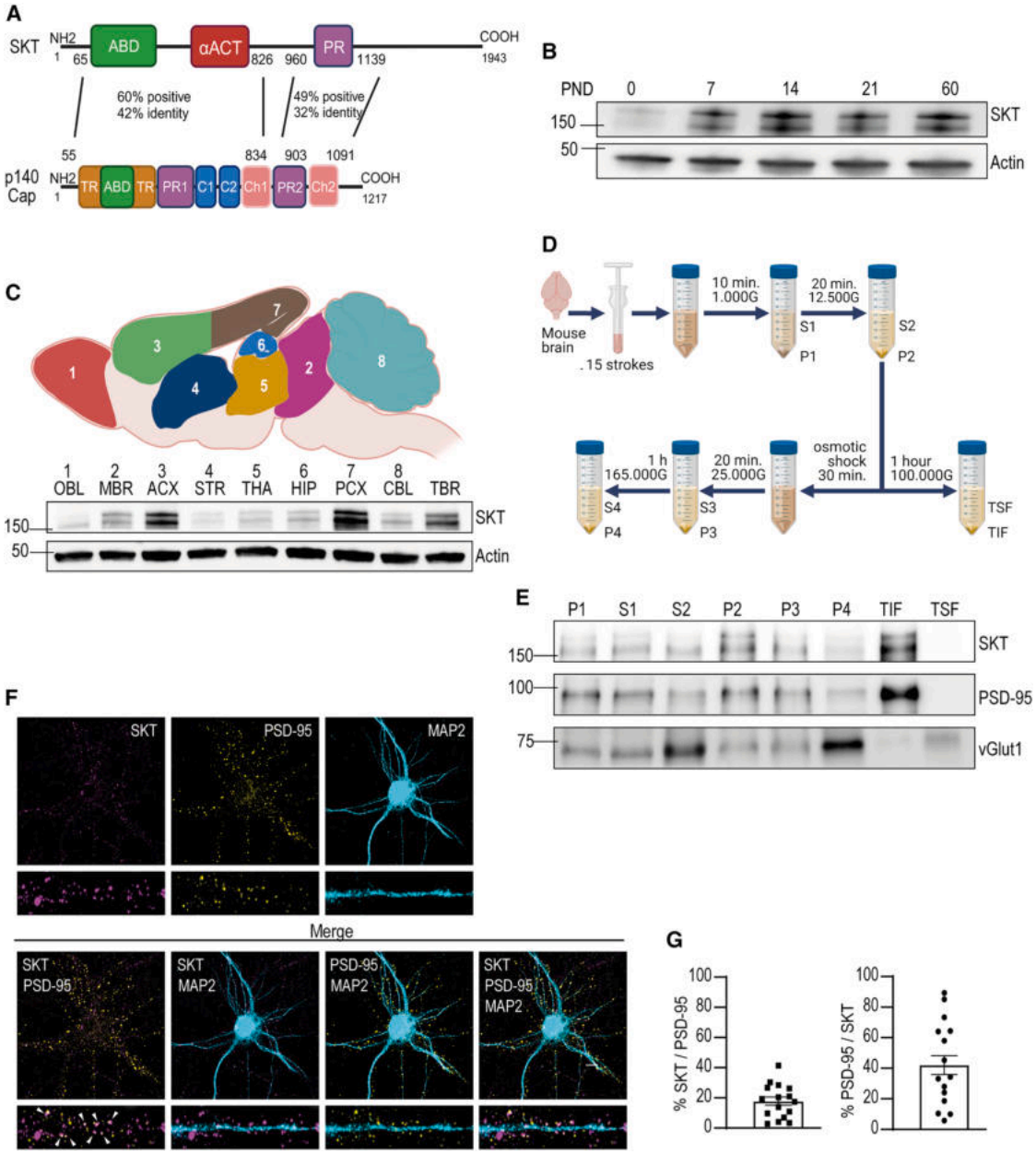

Figure 1. The SKT protein is enriched in the brain postsynaptic compartment

(A) SKT and p140Cap protein structure: percentage of conserved aa substitutions and identity in aa alignment. ABD, ACTIN binding domain; αACT, alpha-ACTIN-like; PR, proline-rich domain; TR, tyrosine-rich domain; C1 and C2, coiled-coil domains; Ch1 and Ch2, charged aa-rich regions.

(B) SKT time-course expression: WB of mouse brain protein extracts (50 μg/lane) at the indicated postnatal days (PND). ACTIN, loading control.

(C) Brain regions: 1, OBL, olfactory bulb; 2, MBR, midbrain; 3, ACX, anterior cortex; 4, STR, striatum; 5, THA, thalamus; 6, HIP, hippocampus; 7, PCX, posterior cortex; 8, CBL, cerebellum; TBR, total brain. Created with BioRender. WB of the indicated brain regions (30 μg/lane). ACTIN, loading control.

(D) Synaptosome preparation steps. P1, nuclear fraction; S1, cytosolic fraction; S2, microsomal fraction; P2, crude synaptosome; P3, minor presynaptic fraction; P4, purified presynaptic vesicles; TIF, Triton-insoluble fraction; TSF, Triton-soluble fraction. Created with BioRender.

(E) WB of fractions described in (D) (30 μg/lane). PSD-95, postsynaptic marker; vGLUT1, presynaptic marker.

(F) Primary neurons at DIV 18 stained for SKT (in magenta), PSD-95 (in yellow), and MAP2 (in cyan). Lower images show the merge of the different antibody combinations. Small images show magnification of 30 μm dendrite segments. Arrowheads, colocalization of PSD-95 puncta with SKT. Scale bar, 10 μm.

(G) Left: percentage of SKT-positive puncta colocalizing with PSD-95 in 30 μm dendrite segments (41.6% ± 8.6%). Right: percentage of PSD-95-positive puncta colocalizing with SKT (18.4% ± 3.1%). Data are represented for n = 2 dendrites/5 neurons/3 embryos for a total of n = 30 dendrite segments.

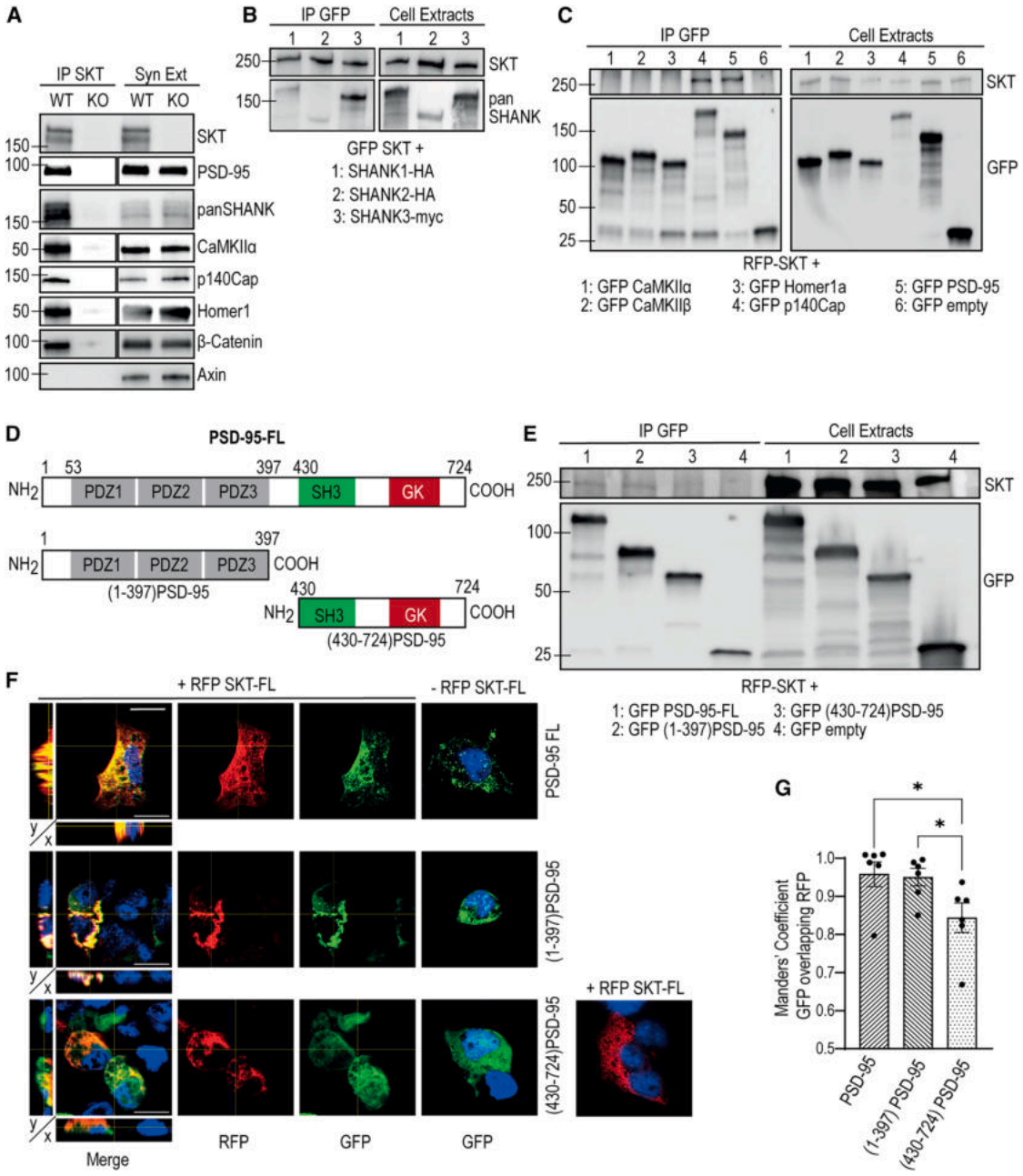

Figure 2. Analysis of SKT interaction with the adaptor proteins PSD-95 and SHANK3

(A) SKT immunoprecipitation from 1 mg brain crude synaptosomes and related synaptosomal extracts (30 μg) as input control. *SKT*-knockout (KO) synaptosomes were used as negative control. $n = 5$ mice.

(B) HEK293T cells were transfected with GFP-SKT plasmid and SHANK 1, 2, or 3 plasmids. GFP immunoprecipitation from 1 mg protein extract and 30 μg/lane was used as input control. $n = 3$.

(C) HEK293T cells were transfected with RFP-SKT-FL plasmid together with the indicated plasmids. GFP immunoprecipitation from 1 mg protein extract and 30 μg/lane was used as input control. $n = 3$.

(D) Schematic illustration of plasmids encoding GFP-PSD-95-FL and its fragments with specific domains.

(E) HEK293T cells were transfected with RFP-SKT-FL plasmids with GFP-PSD-95-FL or the two PSD-95 subdomains. GFP immunoprecipitation from 1 mg protein extract and 30 μg/lane was used as input control. $n = 3$.

(F) Confocal imaging of COS-7 cells cotransfected with RFP-SKT-FL plasmid and GFP-PSD-95-FL or one of two PSD-95 subdomains. The images designated x and y represent the orthogonal view. Scale bars, 10 μm.

(G) Manders' colocalization coefficient (MCC) of GFP-PSD-95 as the average of individual cell quantification. FL is at 0.9583, (1–397) is at 0.9503, and (430–724) is at 0.8840. *$p < 0.05$, one-way ANOVA. Welch's unpaired t test. $n = 2$ individual cells/3 independent experiments.

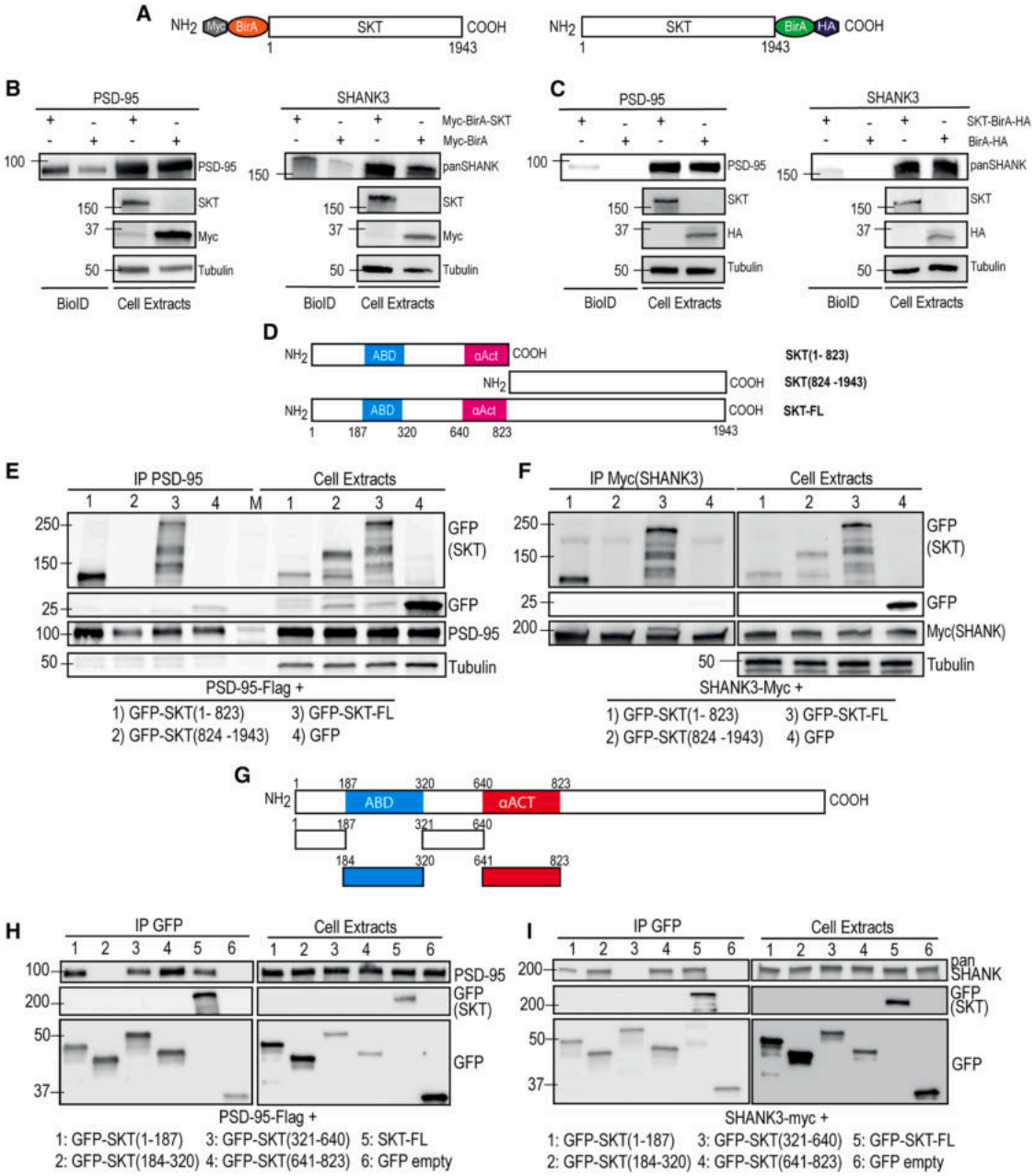

Figure 3. The amino-terminal region of SKT is involved in binding to PSD-95 and SHANK3 in HEK293T cells

(A) SKT-BirA fusion proteins used in the BioID assay.

(B and C) BioID assay in HEK293T. (B) HEK293T cells were cotransfected with Myc-BirA-SKT plasmids and FLAG-PSD-95 or Myc-SHANK3 plasmids. Empty Myc-BirA, negative control. WB of biotinylated proteins (500 μg) and 30 μg cell extracts used as input control. TUBULIN, loading control. $n = 3$. (C) HEK293T cells were cotransfected with SKT-BirA-HA plasmids and FLAG-PSD-95 or Myc-SHANK3 plasmids. Empty BirA-HA, negative control. WB of biotinylated proteins (500 μg) and 30 μg cell extracts used as input control. TUBULIN, loading control. $n = 3$.

(D) GFP-SKT-FL and SKT amino-terminal (1–823) and carboxy-terminal (824–1943) regions.

(E) HEK293T cells were transfected with plasmids shown in (D) and FLAG-PSD-95-FL. M, molecular weight marker. PSD-95 immunoprecipitation from 1 mg protein extract and 30 μg/lane as input control. Lower bands in lane 3 are due to a partial degradation of the GFP-SKT-FL protein. $n = 3$.

(F) HEK293T cells were transfected with plasmids shown in (D) and Myc-SHANK3 plasmids. Myc immunoprecipitation from 1 mg protein extract and 30 μg/lane as input control. Lower bands in lane 3 are due to a partial degradation of the GFP-SKT-FL protein. $n = 3$.

(G) GFP-SKT-FL and four amino-terminal region subdomains.

(legend continued on next page)

with GFP-SKT-FL, GFP-SKT(1–823), or GFP-SKT(824–1,943) with either PSD-95 or SHANK3. The immunofluorescence analysis in COS-7 cells showed that both GFP-SKT-FL and GFP-SKT(1–823) distributed with PSD-95 or SHANK3 with a punctate pattern throughout all the cell (Figures S4A and S4B), compared to GFP-SKT(824–1,943), confirming the biochemical data. Overall, SKT mainly interacts with PSD-95 and SHANK3 through its amino-terminal domain (1–823), strongly suggesting its direct interaction with these proteins.

We further dissected the SKT(1–823) region by generating four GFP-tagged constructs encoding aa 1–187, 184–320, 321–640, and 641–823 (Figure 3G). The constructs were transfected into HEK293T cells together with PSD-95 (Figure 3H) or SHANK3 (Figure 3I). PSD-95 was mainly detected in the coimmunoprecipitation of GFP-SKT(1–187), (321–640), and (641–823) (Figure 3H). In contrast, in Figure 3I, SHANK3 immunoprecipitated mainly with GFP-SKT(184–320) and (641–823), less with (1–187), and not with (321–640). The immunofluorescence analysis in COS-7 cells confirmed that GFP-SKT-FL and only GFP-SKT(321–640) and (641–823) distributed with PSD-95 in specific regions of high density of expression, matching the biochemical data (Figure S5A). In contrast, GFP-SKT(1–187) coimmunoprecipitated in HEK293T cells, but its localization in COS-7 cells was limited to tiny regions of expression, with low Manders' colocalization coefficients (MCCs) (Figure S5A). Consistent with the biochemical analysis, SHANK3 localized with GFP-SKT-FL and regions (641–823) and (184–320) but not with (321–640) (Figure S5B). Overall, SKT interacts with PSD-95 and SHANK3 through distinct parts of its amino-terminal region, only partially overlapping, suggesting that these interactions could be relevant for the development of DSs.

SKT regulates the number and morphology of DSs *in vitro* and *in vivo*

We generated *SKT*-KO mice by inserting a neomycin cassette within exon 7 of the *SKT* gene (see STAR Methods and Figure S6A). Ablation of the SKT protein was verified on brain extracts from *SKT*-KO mice by western blot (WB) (Figure S1B, left) and immunofluorescence analysis (Figure S6B). *SKT*-KO mice were vital, born at a Mendelian ratio, and their lifespan was like that of the WT littermates. KO mice exhibit the characteristic "sickle tail" phenotype (Figure S4C).[16]

Primary hippocampal neurons from WT and *SKT*-KO E18.5 embryos were analyzed at DIV 16 by immunostaining the PSD-95 puncta to identify mature synaptic contacts (Figure 4A). A significantly reduced area of PSD-95 puncta (Figure 4B) and reduced PSD-95 integrity density (Figure 4C) were observed in *SKT*-KO neurons compared to WT. Moreover, the number of PSD-95 puncta with a size over 0.5 μm^2, likely more mature DSs, was decreased (Figure 4D).[23]

To further study DS morphology and number in primary neurons, we transfected neurons at DIV 14 with a GFP empty vector to fill the dendritic shaft and DSs (Figure 4E). DSs were classified as filopodia, stubby, and mushroom-like based on their size and shape (Figure 4F). *SKT*-KO neurons displayed a significant decrease in total DS density compared to WT, with a decrease in mushroom-like spines and an increase in filopodia (Figure 4G). Moreover, the percentage of filopodia was significantly increased in *SKT*-KO neurons, with a parallel decrease in mushroom-like spines (Figure 4H). Overall, the absence of SKT is correlated with defective spine production and maturation.

A rescue experiment was performed by expressing exogenous SKT in *SKT*-KO primary neurons. Plasmids expressing GFP-tagged SKT or GFP under the *SYNAPSIN1* promoter (*SYN1::GFP-SKT* or *SYN1::GFP*) were magnetofected into *SKT*-KO primary neurons. Confocal microscopy (Figure 4I) showed that *SYN1::GFP-SKT* rescued the DS density in KO cells and significantly restored the mushroom morphology, with a concomitant decrease in filopodia (Figure 4J). Similarly, a plasmid encoding *SYN1::GFP-SKT*amino-terminal(1–823) was generated and magnetofected into *SKT*-KO primary neurons (Figure 4K). Its expression rescued the total DS density (Figure 4L) and significantly restored the mushroom morphology, with a concomitant, statistically significant decrease in filopodia but less pronounced compared to the rescue with the FL protein (Figure 4L). Therefore, in KO primary neurons, expression of SKT and of its amino-terminal 1–823 region is sufficient to rescue both number and morphology of mushroom DS.

The *Thy1-GFP/M* transgenic mice express the GFP protein under the *Thy1* promoter (*Thymocyte differentiation antigen 1*) in several neuronal subsets, including cortical excitatory neurons.[24] By breeding *SKT*-heterozygous mice with *SKT*-heterozygous mice carrying *Thy1-GFP/M*, we obtained WT and KO littermates, both expressing GFP. Confocal analysis was performed on 80 μm primary dendrite segments (Figure 5A). To avoid any bias, the density and the shape of the DSs were automatically analyzed using a Python algorithm to measure the length of the neck (l) and the width of the head (w) to classify DSs (Figures 5B and S7). A significant decrease in DS density in *SKT* KO compared to WT was found, as illustrated in the scatterplot (Figure 5C) and in the bar chart (Figure 5D), with no concomitant change in the distribution of each spine morphology in KO vs. WT mice (Figure 5E). Altogether, our *in vitro* and *in vivo* analyses point out that SKT regulates spine density and morphology, likely producing its effect in different steps of neuronal development.

Dynamic remodeling of the ACTIN cytoskeleton is essential for DS shape and maturation[25] through a complex network of signaling molecules,[26,27] including small GTPases and their regulators. PSD-95 functions to organize synaptic Rac1 signaling in a multiprotein complex,[28] and dysregulation of all SHANK isoforms, especially SHANK3, leads to alterations in DSs and in synapse activity by altering ACTIN dynamics.[29] By pull-down and WB from synaptosomes, *SKT*-KO mice displayed increased levels of active RHOA (Figure 5F), decreased levels of RAC1 (Figure 5G), and increased levels of Ser-3 PHOSPHOCOFILIN (Figure 5H) compared to WT. Indeed, activated RHOA is known to impair DS remodeling by inhibiting COFILIN through phosphorylation on

(H) HEK293T cells were transfected with plasmids shown in (G) and FLAG-PSD-95-FL. GFP immunoprecipitation from 1 mg protein extract and 30 μg/lane as input control. $n = 3$.

(I)HEK293T cells were transfected with plasmids shown in (G) and Myc-SHANK3. GFP immunoprecipitation from 1 mg protein extract and 30 μg/lane as input control. $n = 3$.

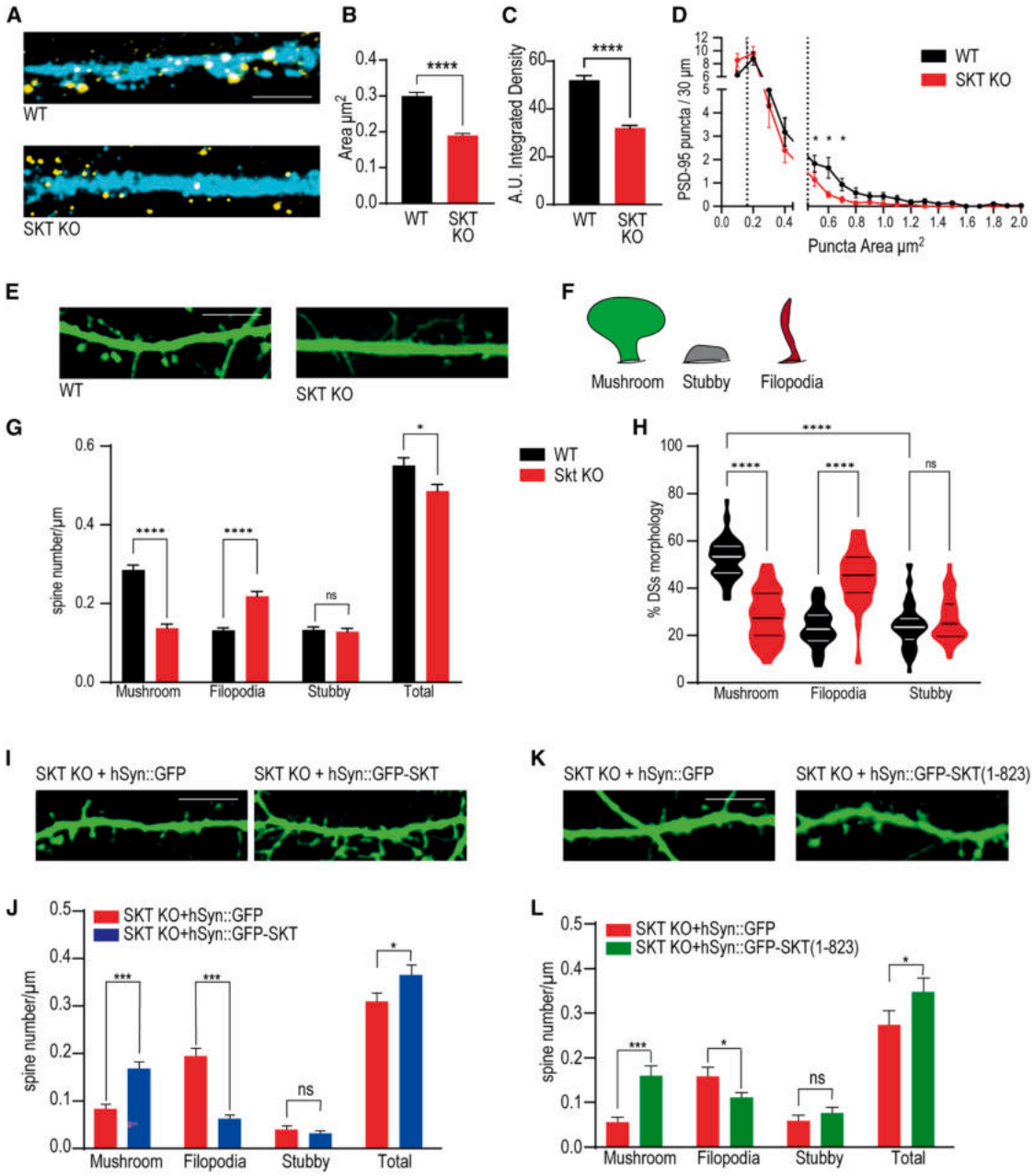

Figure 4. *In vitro* analysis of dendritic spines in primary neuronal cultures

(A–D) WT and *SKT*-KO primary neurons at DIV 16 were stained with PSD-95 (in yellow) and MAP2 antibodies (in cyan). (A) Representative confocal images of PSD-95-positive puncta on a 30 µm dendrite. Scale bar, 10 µm. (B) PSD-95 punctum area quantification. Welch's unpaired t test. ****$p < 0.0001$. (C) Quantification of PSD-95 punctum integrity density in arbitrary units (A.U.). Welch's unpaired t test. ****$p < 0.0001$. (D) PSD-95 punctum area frequency distribution. Welch's unpaired t test. *$p < 0.05$. Two dendrites/five neurons/three embryos. $n = 30$ dendrite segments.

(E–H) WT and *SKT*-KO primary neurons were transfected at DIV 14 with pEGFP plasmid. (E) Confocal images of 30 µm GFP-filled dendrites. Scale bar, 10 µm. (F) Shapes of spines: mushroom, filopodia, and stubby. (G) Frequency distribution of DS density based on the shape on 30 µm dendrites; WT $n = 2$ dendrites/8 neurons/4 embryos, $n = 64$ segments; KO $n = 2$ dendrites/6 neurons/3 embryo, $n = 37$ segments. Mushroom: 0.29 ± 0.01 spine/µm WT vs. 0.14 ± 0.06 spine/µm *SKT* KO, ****$p < 0.0001$. Filopodia: 0.13 ± 0.05 spine/µm WT vs. 0.22 ± 0.07 spine/µm *SKT* KO, ****$p < 0.0001$. Stubby: 0.13 ± 0.06 spine/µm WT vs. 0.13 ± 0.05 spine/µm *SKT* KO, ns, not significant. Total: 0.55 ± 0.016 spine/µm WT vs. 0.48 ± 0.11 spine/µm, *$p < 0.05$, Welch's unpaired t test. (H) Percentage of distribution of different types of spines: $n = 64$ WT, $n = 37$ *SKT* KO. Mushroom: 51.83% ± 1.12% WT vs. 28.19% ± 1.78% *SKT* KO, ****$p < 0.0001$. Filopodia: 23.6% ± 0.99% WT vs. 44.98% ± 1.87% *SKT* KO, ****$p < 0.0001$. Stubby: 23.9% ± 1.1% WT vs. 26.8% ± 1.5% *SKT* KO, ns, not significant. Two-way ANOVA with Bonferroni correction.

(I and J) Rescue experiments in *SKT*-KO primary neurons magnetofected at DIV 14 with *SYN1*::GFP-SKT or *SYN1*::GFP. (I) Confocal images of DSs. Scale bar, 10 µm. (J) Frequency distribution of DS density; 30 µm dendrite length; *SYN1*::GFP $n = 2$ dendrites/5 neurons/4 embryo, $n = 41$ segments; *SYN1*::GFP-SKT $n = 2$ dendrites/6 neurons/3 embryos, $n = 37$ segments. Spine/µm: mushroom, 0.08 ± 0.01 *SYN1*::GFP vs. 0.17 ± 0.01 *SYN1*::GFP-SKT; filopodia, 0.19 ± 0.01

(legend continued on next page)

Ser-3 by the ROCK/LIMK pathway.[30] Altogether, the wide DS rearrangement produced by SKT loss may be caused by abnormal levels of small GTPase activity influencing ACTIN polymerization.

SKT modulates spontaneous firing and network synchronization in primary neuronal cultures

Hippocampal neurons on microelectrode arrays (MEAs) show time-dependent changes in firing, with immature cultures displaying sparse bursts that become more synchronized as they mature.[31–34] To investigate the role of SKT in electrophysiological neuronal properties, we recorded MEA activity from DIV 7 to DIV 18 in nine WT and *SKT*-KO hippocampal cultures (each from a single embryo).[33] At DIV 7, *SKT*-KO neurons showed significantly fewer bursts and lower mean frequency (Figures S8A–S8C), with no difference in burst duration (Figure S8D) or the percentage of silent channels (Figure S8E). At DIV 18, *SKT*-KO neurons still showed reduced burst number, burst frequency, and burst duration (Figures S8F–S8I), along with more silent channels (Figure S8J).

The MEA raster plots at DIV 18 revealed decreased synchronization in *SKT*-KO cultures compared to WT (Figure S8K), confirmed by a reduced cross-correlation peak (Figures S8L–S8M), indicating impaired network synchrony. Overall, the MEA analysis revealed in *SKT*-KO networks the typical features of immature cultures, with a significant delay in neuronal synchronization.

SKT decreases both the amplitude and the frequency of mEPSCs

The role of SKT in synaptic function was examined by electrophysiological recordings in hippocampal slices. We first analyzed miniature excitatory postsynaptic currents (mEPSCs) from CA1 pyramidal neurons in P60 WT and *SKT*-KO mice (Figure 6A). In *SKT*-KO neurons, the mean amplitude of mEPSCs was significantly reduced (−17.83 ± 0.33 pA in WT vs. −9.11 ± 0.15 pA in *SKT* KO), and the mean interevent interval (IEI) of mEPSCs was prolonged (504.7 ± 14.2 ms in WT vs. 1,557.0 ± 61.8 ms in *SKT* KO; Figures 6A–6C), with no change in rise or decay kinetics. Cumulative plots showed a leftward shift in amplitude and a rightward shift in IEIs. To assess whether SKT affects α-amino-3-hydroxy-5-methyl-4-isoxazolepropionic acid receptor (AMPAR) number or unitary current, we performed peak-scaled variance analysis (PSVA) of mEPSCs.[35,36]

The parabolic relationship between variance (σ^2) and average amplitude of mEPSCs was altered in *SKT* KO (Figure 6D). Both the initial slope (*i*, unitary current) and the parabola width (*N i*) were reduced, indicating a decrease in *i* from 1.8 ± 0.3 pA in WT to 0.8 ± 0.1 pA in *SKT*-KO mice (Figure 6E). However, receptor number (*N*), then estimated by dividing the width (*N i*) by *i*, was unchanged (10.4 ± 1.1 in WT and 12.5 ± 1.2 in *SKT*-KO mice) (Figure 6F). Thus, SKT loss markedly increases IEI and reduces AMPAR conductance, without altering receptor number per quantum.

SKT loss decreases the amplitude of evoked EPSCs and the size of the synchronous readily releasable pool while preserving the release probability during high-frequency stimulation

We recorded evoked EPSCs (eEPSCs) in CA1 pyramidal neurons (SC-CA1) by stimulating the Schaffer collaterals in both WT and *SKT*-KO mice (Figure 6G). The amplitude of eEPSCs was significantly reduced in *SKT*-KO neurons compared to WT controls (−191 ± 21 pA vs. −105 ± 11 pA; Figure 6H). This ∼50% decrease in eEPSCs is consistent with the reduction observed in mEPSC amplitude (Figure 6E), suggesting a postsynaptic contribution.

To assess presynaptic involvement, we examined paired-pulse facilitation (PPF), which reflects changes in vesicle release probability (*Pves*). Using increasing interstimulus intervals (ISIs), we measured the paired-pulse ratio (PPR) at SC-CA1 synapses (Figure 6I). WT synapses showed typical facilitation (51.2% at 25 ms and 46.8% at 50 ms) decaying to ∼15% by 200 ms (τ = 49 ms; Figure 6J). In *SKT*-KO synapses, PPRs were significantly higher at short ISIs (99.9% at 25 ms and 78.0% at 50 ms) but decayed similarly (steady state ∼18%, τ = 51 ms; Figure 6J). These findings indicate that, while basal *Pves* is similar, enhanced facilitation in *SKT*-KO neurons suggests that increased presynaptic Ca^{2+} buildup during brief intervals may elevate *Pves* during high-frequency activity.

To further investigate presynaptic function, we applied a 20 Hz stimulus train for 2 s to assess both the size of the synchronous readily releasable pool (RRPsyn) and the efficiency of sustained vesicle release (Figures 6K and 6L). We observed a significant reduction in RRPsyn in *SKT*-KO neurons (−3.17 ± 0.65 nA) compared to WT (−8.02 ± 0.65 nA) (Figure 6M). However, the vesicle release probability (Pves), calculated by dividing the average eEPSC amplitude by RRPsyn, was not significantly different between the groups (0.04 ± 0.01 in WT vs. 0.04 ± 0.02 in *SKT* KO; Figure 6N).

In conclusion, SKT loss leads to a significant reduction in excitatory synaptic transmission in CA1 neurons, primarily due to a marked decrease in the size of RRPsyn and reduced postsynaptic AMPAR-mediated quantal responses. These combined pre- and postsynaptic alterations account for the impaired synaptic efficacy observed in *SKT*-KO mice.

SKT-KO mice exhibit repetitive behavior and motor, cognitive, and executive deficits

WT and *SKT*-KO mice were subjected to a comprehensive series of standard behavioral tests, including: (1) the nesting and

*SYN1::*GFP vs. 0.06 ± 0.01 *SYN1::*GFP-SKT; stubby, 0.04 ± 0.01 *SYN1::*GFP vs. 0.03 ± 0.01 *SYN1::*GFP-SKT; total, 0.31 ± 0.02 spine/μm *SYN1::*GFP vs. 0.36 ± 0.02 spine/μm *SYN1::*GFP-SKT. ns, not significant; *$p < 0.05$; and ***$p < 0.001$. Welch's unpaired t test.

(K and L) Rescue experiments in *SKT*-KO primary neurons, magnetofected at DIV 14 with *SYN1::*GFP-SKT amino-terminal(1–823) or *SYN1::*GFP. (K) Confocal images of DSs. Scale bar, 10 μm. (L) Frequency distribution of DS density; 30 μm dendrite length; *SYN1::*GFP n = 2 dendrites/2 neurons/3 embryos; n = 12 *SYN1::*GFP; n = 13 *SYN1::*GFP-SKT amino-terminal(1–823). Spine/μm: mushroom, 0.06 ± 0.01 *SYN1::*GFP vs. 0.17 ± 0.02 *SYN1::*GFP-SKT amino-terminal(1–823); filopodia, 0.16 ± 0.02 *SYN1::*GFP vs. 0.11 ± 0.01 *SYN1::*GFP-SKT amino-terminal(1–823); stubby, 0.06 ± 0.01 *SYN1::*GFP vs. 0.08 ± 0.01 *SYN1::*GFP-SKT amino-terminal(1–823) *P*; total, 0.26 ± 0.02 *SYN1::*GFP vs. 0.34 ± 0.03 *SYN1::*GFP-SKT amino-terminal(1–823). *$p < 0.05$, ***$p < 0.001$, and ns, not significant. Welch's unpaired t test.

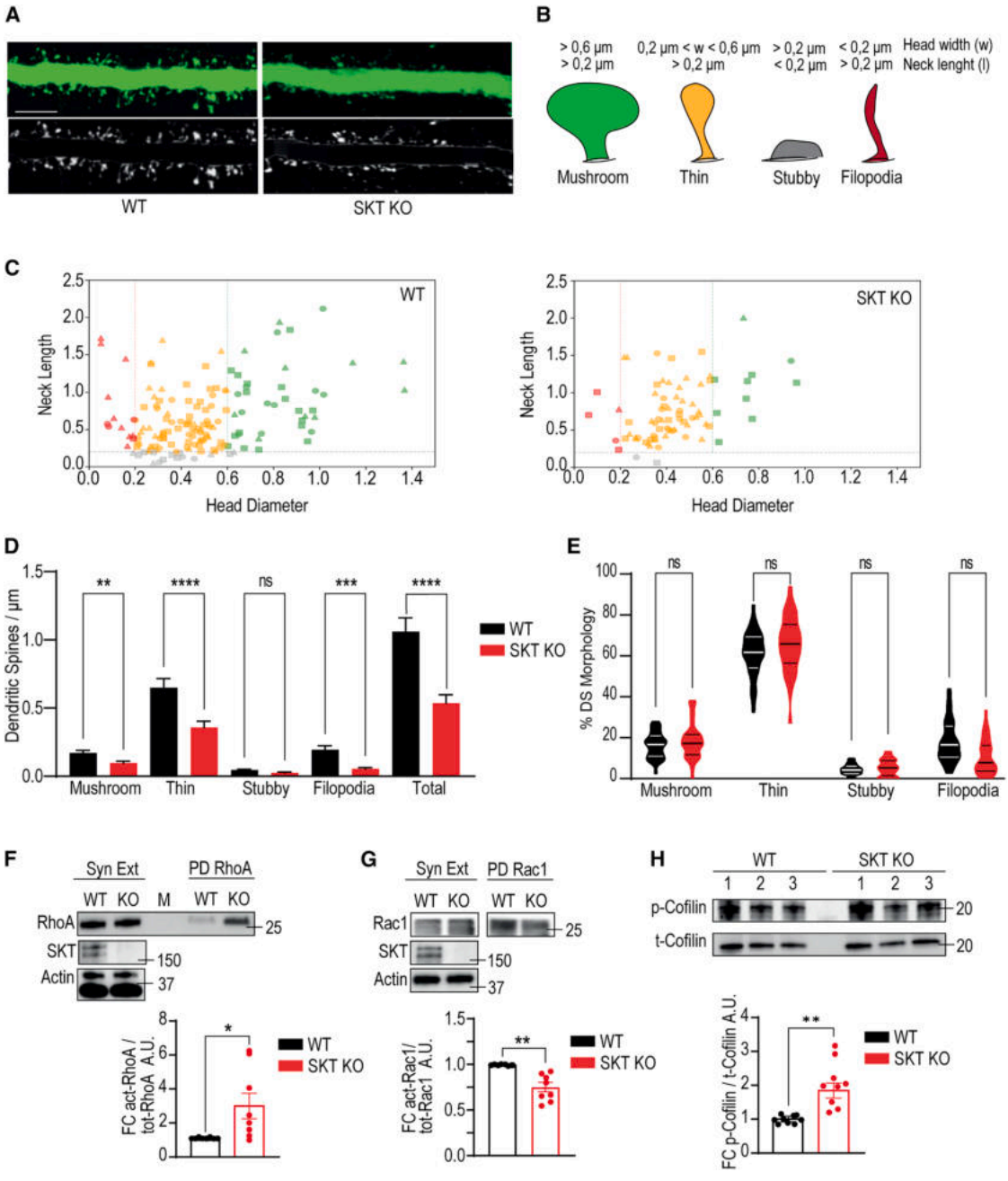

Figure 5. *In vivo* analysis of dendritic spines

(A) Confocal images of 80-µm-long primary dendrite segments from P60 WT and *SKT*-KO cortical pyramidal neurons; 5 mice, 10 slices/mouse, 5 neurons/slice, and $n = 1$ dendrite/neuron.

(B) Classification of DS based on the neck length (l) and head width (w).

(C) Scatterplot of DS WT and *SKT*-KO *Thy1::GFP*, counted and classified according to the Python algorithm based on length (l) and head width (w). Colored symbols indicate different DS morphologies, as illustrated in (B). Different-shaped symbols indicate the DS morphologies of three different representative mice.

(D) DS density analysis in WT and *SKT* KO classified on their morphology. Spine/µm: mushroom, 0.19 ± 0.05 in WT vs. 0.1 ± 0.08 in *SKT* KO; thin, 0.68 ± 0.22 in WT vs. 0.37 ± 0.22 in *SKT* KO; stubby, 0.08 ± 0.02 in WT vs. 0.06 ± 0.02 in *SKT* KO; filopodia, 0.23 ± 0.15 in WT vs. 0.1 ± 0.08 in *SKT* KO; total, 1.3 ± 0.3 in WT vs. 0.6 ± 0.1 in *SKT* KO. $^{**}p < 0.01$, $^{***}p < 0.001$, $^{****}p < 0.0001$, and ns, not significant; unpaired t test. Error bars correspond to ±SD.

(E) Percentage of DS different morphologies (mushroom, 16.3 ± 1.03 in WT vs. 18.4 ± 1.7 in *SKT* KO; thin, 61.2 ± 1.9 in WT vs. 65.7 ± 2.3 in *SKT* KO; stubby, 4.4 ± 0.4 in WT vs. 5.2 ± 0.7 in *SKT* KO; filopodia, 18.0 ± 1.7 WT vs. 10.6 ± 1.4 in *SKT* KO). Error bars correspond to ±SEM. Unpaired t test, ns, not significant.

(legend continued on next page)

burrowing assays, indicators of activities of daily living (ADL)[37]; (2) the open field (OF) test, for locomotor and exploratory activity; (3) the elevated plus maze (EPM), for anxiety-like behavior; (4) the novel object recognition (NOR) test, for short-term recognition memory; (5) the rotarod test, for motor coordination and balance; (6) the Barnes maze (BM), for spatial long-term memory; and (7) the puzzle box (PB) test, to assess problem-solving skills linked to cognitive behavior and executive functioning.

No significant differences in ADL were observed between genotypes. However, *SKT*-KO mice failed to display a characteristic overnight increase in burrowing activity compared to the initial 2 h and their WT controls (Figure 7A).

No differences were detected between genotypes regarding total distance traveled and percentage of time spent in the center of the OF arena. However, *SKT*-KO mice spent significantly more time than WT in self-grooming behavior, indicative of increased stereotypic activity (Figure 7B). Repetitive and intense motor activity is often accompanied by a reduction in overall locomotion. In agreement, *SKT*-KO mice exhibiting high grooming durations demonstrated reduced distance traveled. OF locomotor and exploratory activity was further analyzed in Figure S9A.

The total arm entries in the EPM, as well as the percentage of entries and time spent in the open arms, were comparable between groups (Figure 7C).

Nevertheless, *SKT*-KO mice had a significant deficit in discriminating the novel object in the NOR test (Figure 7D) and showed shorter latency to fall from the accelerating rotating bar compared to WT mice on each day of rotarod testing for a 2 day session (Figure 7E).

In the BM,[38] no differences emerged between genotypes in the latency to locate the target hole, and both groups improved their performance across training days. However, by analyzing separately each learning day, a significant effect between groups emerged at day 3, suggesting faster acquisition for *SKT* KO (Figure 7F, left).

On the probe trial, statistical analysis revealed again no effect of genotype but a significant effect of genotype-quadrants interaction. Indeed, *SKT* KO spent less time in zone 4 in favor of the target zone (Figure 7F, middle). A higher persistence of a portion of *SKT* KO for the target zone during the probe trial might be interpreted as lower cognitive flexibility.[39] However, both WT and *SKT* KO showed similar abilities in finding the new target location in a reversal task (Figure 7F, right). Overall, Barnes' test indicates an intact spatial reference memory in *SKT*-KO mice.

The PB test evaluates the mouse's ability to solve increasingly complex tasks and the capacity to remember the solutions for subsequent trials.[38] Latencies in solving the tasks were higher for *SKT*-KO mice compared to WT on the first presentation of the new task in the first 2 days (tasks 2.1 and 3.1), but an improvement for both genotypes was observable when the tasks were represented (tasks 2.2, 2.3, and 3.2) (Figure 7G, left). However, despite this initial proactive approach, when faced with more challenging tasks (by day 3), *SKT*-KO mice showed worse performance. Indeed, the latency of task 3.3 resulted significantly differently (percentage of success: 70% for WT vs. 36% for *SKT* KO). Interestingly, at the first presentation of the last, most difficult task (4.1), both genotypes showed the highest latency, probably due to a fearful reaction to the newly inserted object (a plug). In the following tasks, however, only WT mice started to approach the plug to remove it and pass to the other side, and the percentage of success at the last task (4.3) was 70% for WT mice against only 27% for KO. Overall, the mean latency of all tasks was higher for *SKT*-KO mice, which therefore performed significantly worse than WT (Figure 7G, middle). For more details regarding *SKT*-KO behavior in this test, see Figure S9B.

DISCUSSION

Here, we demonstrate that SKT localizes in the PSD, where it interacts with PSD-95 and SHANK3, participating in two fundamental DS networks, one containing PSD-95 localized at the proximal membrane domain and the second recruiting SHANK3 and extending to the inner part of the DS. *SKT*-KO mice exhibit a decreased DS density, with a propensity for less mature morphologies; display reduced miniature and evoked EPSCs; and show alterations in many behavioral domains.

Alterations in DS density and morphology, key indicators of synaptic maturation and function, are prevalent in neuropsychiatric disorders like autism spectrum disorders and schizophrenia.[40,41] In *SKT*-KO mice, we observed increased immature filopodia and decreased mature mushroom spines, reminiscent of phenotypes observed in other PSD-protein-KO models.[8,9] Moreover, we demonstrated that SKT deficiency impairs the RHO-family GTPase signaling pathways, affecting the ACTIN dynamics critical for spine morphogenesis.[10,42–44] The DS defects observed in *SKT*-KO neurons were rescued by expressing full-length SKT protein or its amino-terminal region 1–823, indicating a causal role of SKT in regulating DS morphology and suggesting that PSD-95 and SHANK3 require SKT to appropriately perform in the PSD network.

The *ex vivo* analyses suggest that SKT controls spine density more than their morphological maturation. The differences that we found in DS number and morphology comparing genotypes in primary neurons from embryos or in brain slices from P60 mice could be parsimoniously explained by compensatory mechanisms occurring *in vivo*, such as pruning,[45] which ensures synaptic balance and network stability, essential for proper brain functioning.

The defects in spine morphology observed in *SKT*-KO neurons can be ascribed to abnormal activation of the small GTPases pathways, interfering with RHOA/COFILIN and RAC1 signaling. Moreover, *SKT*-KO neurons show increased phosphorylation of COFILIN, with its shifting to the inactive state, impairing proper DS remodeling.[30,46,47] However, the molecular link between SKT and RHO-family GTPases remains to be determined.

(F and G) Pull-down assay for RHOA and RAC1 activity from WT and *SKT*-KO crude synaptosomes. (F) Fold change (FC) in arbitrary units (A.U.) of RHOA activation. $n = 6$ preparations of synaptosomes for genotype. Paired t test; error bars correspond to ±SEM; $^{*}p < 0.05$. M, MW marker. (G) FC in A.U. of RAC1 activation in $n = 8$ independent preparations of synaptosomes for genotypes. Paired t test; error bars correspond to ±SEM; $^{**}p < 0.01$.
(H) WB analysis of WT or *SKT*-KO synaptosomes. FC in A.U. of p-COFILIN in $n = 9$ mice for genotypes. Paired t test; error bars correspond to ±SEM; $^{*}p < 0.05$ and $^{**}p < 0.01$.

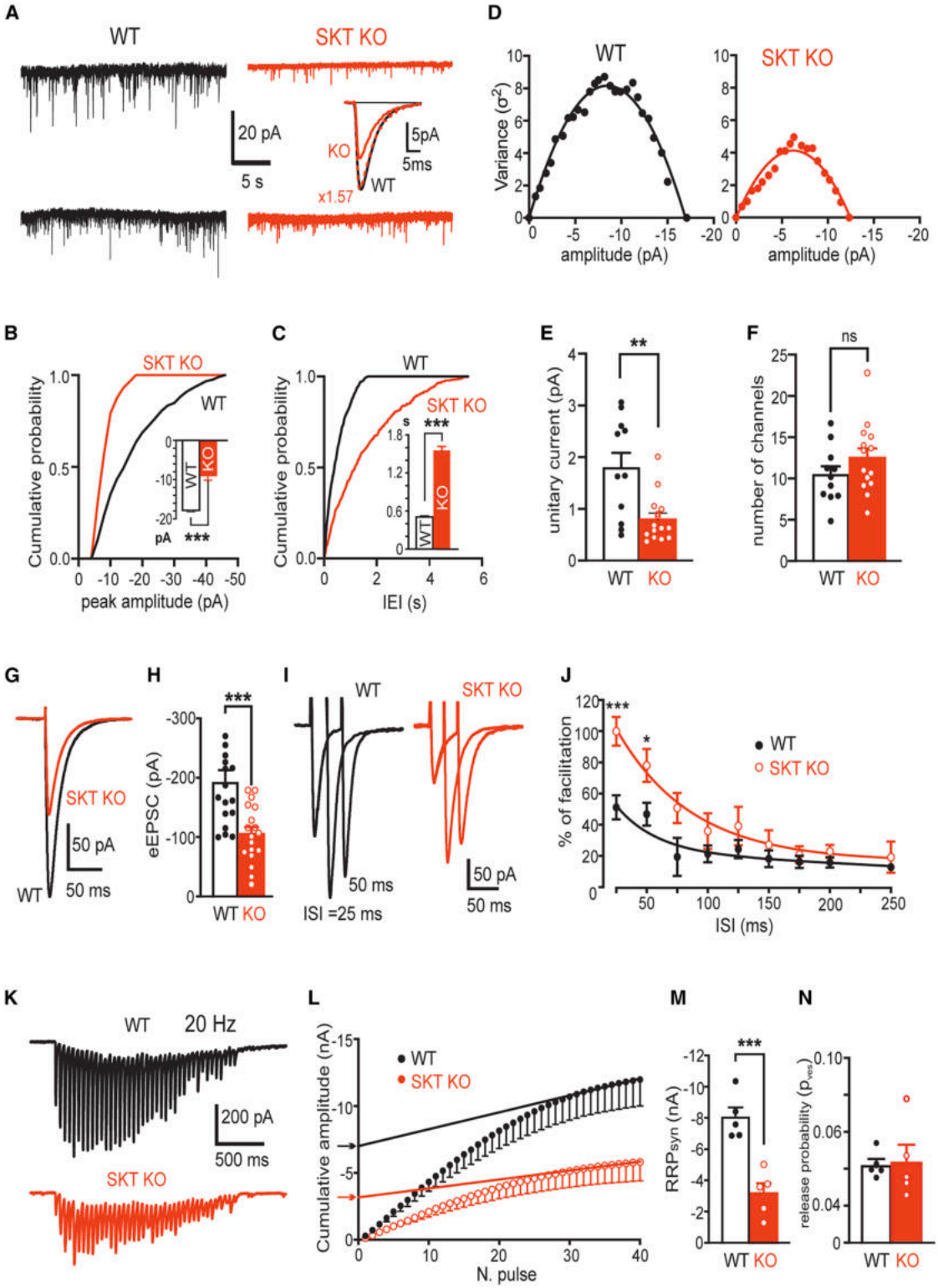

Figure 6. *SKT*-KO hippocampal neurons show impaired excitatory synaptic responses

(A) Representative mEPSCs recorded from CA1 pyramidal neurons in hippocampal slices of WT (black) and *SKT*-KO (red) mice. Averaged mEPSC traces for WT (n = 89, black) and *SKT* KO (n = 25, red) are shown in the inset; the dashed red trace is scaled by 1.57. SKT deletion did not affect activation or decay kinetics. Mean rise times were 2.44 ± 0.17 ms (WT) and 2.69 ± 0.23 ms (KO), and decay times were 6.22 ± 0.60 ms (WT) vs. 5.00 ± 0.48 ms (KO) (n = 11 cells/7 slices for WT, 14 cells/8 slices for KO).

(legend continued on next page)

MEA analysis of *SKT*-KO neurons displays delayed network synchronization during neuronal maturation, consistent with the morphological abnormalities,[31] while MEA experiments in p140Cap KO show a more effective synchronous activity.[32] Indeed, p140Cap, in addition to its role in the postsynaptic excitatory compartment,[10,48] plays a key role in the development and refinement of the inhibitory network.[32] Although SKT and vGAT colocalize along dendritic shafts, no data are currently available on the action of SKT in inhibitory neurons, suggesting that the functional roles of SKT and p140Cap may be different, irrespective of their sequence homology.

The patch-clamp experiments highlight two important effects of SKT loss on excitatory synaptic plasticity. First, SKT loss reduces the quantal size of AMPAR-mediated currents without altering receptor density, likely due to changes in AMPAR subunit composition, requiring future investigation.[49,50] Second, *SKT*-KO neurons show a marked reduction in RRPsyn, while Pves during sustained activity remains unchanged. This synaptic weakening likely contributes to the impaired network synchronization and maturation observed in primary cultures (DIV 7–14).

SKT loss also enhances PPF, a form of short-term plasticity driven ∼50% by Cav2.1 (P/Q-type) channel facilitation via calmodulin (CaM)[51] and ∼50% by Ca^{2+}-independent mechanisms.[52] How the two types of facilitation (Ca^{2+} current dependent and independent) increase in the absence of SKT remains to be clarified, but it is worth noticing that PPF increase is restricted to short ISIs (25–50 ms) (Figures 6I and 6J), suggesting its relevance at high-frequency stimulation (above 20 Hz), where it may partially compensate for reduced *Pves* (Figures 6K–6N). As SKT is absent in presynaptic compartments, these alterations may reflect compensatory presynaptic adaptations to postsynaptic dysfunction.

The morphological and electrophysiological abnormalities observed in *SKT*-KO mice are associated with a complex range of behavioral alterations. *SKT* KO showed impaired motor coordination and pronounced self-grooming, which points to corticostriatal interaction deficits. Interestingly, such deficits are described in *SHANK3*-KO mice,[9] and similar behavioral alterations are displayed by mice with total *PSD-95* deletion.[53]

The negative discrimination index value obtained by *SKT*-KO mice in the NOR suggests working memory alteration,[54] with an inability to distinguish the novel object from the familiar one. Moreover, *SKT*-KO mice showed deficits in executive function and problem solving, as tested in the PB.[38] Interestingly, a study that analyzed common genetic variations in executive function and working memory identified the gene *KIAA1217*, the human homolog of *SKT*, as the best hit for digit-span backward, with a high significance.[55]

The reduced performance in the PB test could also be related to increased avoidance and reduced motivation. Impairments in digging and burrowing activity may also have negatively affected executive abilities. Notably, motor deficits, avoidant behavior, reduced digging bouts, and increased self-grooming are related to the integrity and functionality of brain areas strongly expressing SHANK3 in an isoform-specific manner.[56] Considering the high expression of SKT in the cortex, the results obtained confirm a high involvement of cortical function in the observed deficits. Moreover, according to what was described in *SHANK3*-transgenic mice, spatial learning and memory in the Barnes test were unchanged in *SKT*-KO mice, as well as cognitive flexibility,[56] suggesting no significant impairments in spatial reference memory. Although this may seem counterintuitive given the electrophysiological abnormalities recorded in the hippocampus, it is noteworthy that even the whole-brain genetic depletion of GluA1 is not sufficient to induce alteration of long-term spatial memory, despite the strong impact on α-amino-3-hydroxy-5-methyl-4-isoxazolepropionic acid (AMPA)-dependent currents and hippocampal long-term potentiation (LTP).[57]

Overall, SKT is involved in DS generation and maturation, through its ability to interact with a network of PSD proteins that determines cortical function at the electrophysiological and behavioral levels. Here, we analyzed SKT interaction with the most relevant PSD scaffold proteins, PSD-95 and SHANK3, and provided insights into its role in synaptic signal transduction. These findings lay the groundwork for future investigations into SKT's involvement in neurological disorders and potential therapeutic strategies.

Limitations of the study

In this study, we used total KO of the *SKT* gene to assess its relevance in the synaptic compartment. However, a conditional KO will allow the protein to be deleted in a spatially controlled manner to understand SKT's role in specific compartments.

(B and C) Cumulative distributions of mEPSC amplitudes and interevent intervals (IEIs) in WT (black) and *SKT*-KO (red) hippocampal neurons. Insets show corresponding bar graphs of peak amplitudes and IEIs. Kolmogorov-Smirnov test, ***$p < 0.0001$. The error bars correspond to ±SEM.
(D) Parabolic fits of mEPSC variance (σ^2) vs. amplitude using PSVA in WT and *SKT*-KO neurons. The slope at the origin ("*i*") reflects the AMPAR unitary current, while the second *x* intercept ("*N i*") represents the total current from *N* AMPARs activated by a single neurotransmitter quantum.
(E and F) Bar graphs showing AMPAR unitary current (*i*) (Mann-Whitney test, **$p < 0.01$) and number of receptors (*N*) (unpaired t test, $p = 0.20$) derived from parabolic fits in WT and *SKT*-KO hippocampal neurons. The error bars correspond to ±SEM. $n = 11$ cells/7 slices/WT and 14 cells/8 slices/*SKT*-KO mice.
(G and H) Representative and averaged eEPSC traces recorded at SC-CA1 synapses in WT and *SKT*-KO neurons ($n = 17$ cells/3 slices for WT; 18 cells/4 slices for *SKT* KO). Mann-Whitney test, ***$p < 0.001$. The error bars correspond to ±SEM.
(I) Paired-pulse facilitation of eEPSCs at 25 and 50 ms ISIs in WT (black) and *SKT*-KO (red) neurons ($n = 12$ cells/5 slices for WT; 9 cells/5 slices for *SKT* KO).
(J) Mean PPF (%) across ISIs (25–250 ms) in WT (filled black circles) and *SKT*-KO (open red circles) neurons. Unpaired t test, *$p < 0.05$ and ***$p < 0.0001$. The error bars correspond to ±SEM.
(K) Representative eEPSC traces during 20 Hz stimulation for 2 s in WT and *SKT*-KO hippocampal neurons.
(L) Cumulative eEPSC amplitudes during 20 Hz trains in WT and *SKT*-KO neurons. Linear fits of the 30th to the 40th pulse were back-extrapolated to estimate RRPsyn (arrows). $n = 5$ cells/5 slices per group.
(M and N) Bar graphs showing mean RRPsyn size and vesicle release probability (Pves) in WT and *SKT*-KO neurons. SKT deletion significantly reduces RRPsyn (8,021 vs. 3,169 pA) with no notable change in Pves. Mann-Whitney test, ***$p < 0.001$. The error bars correspond to ±SEM.

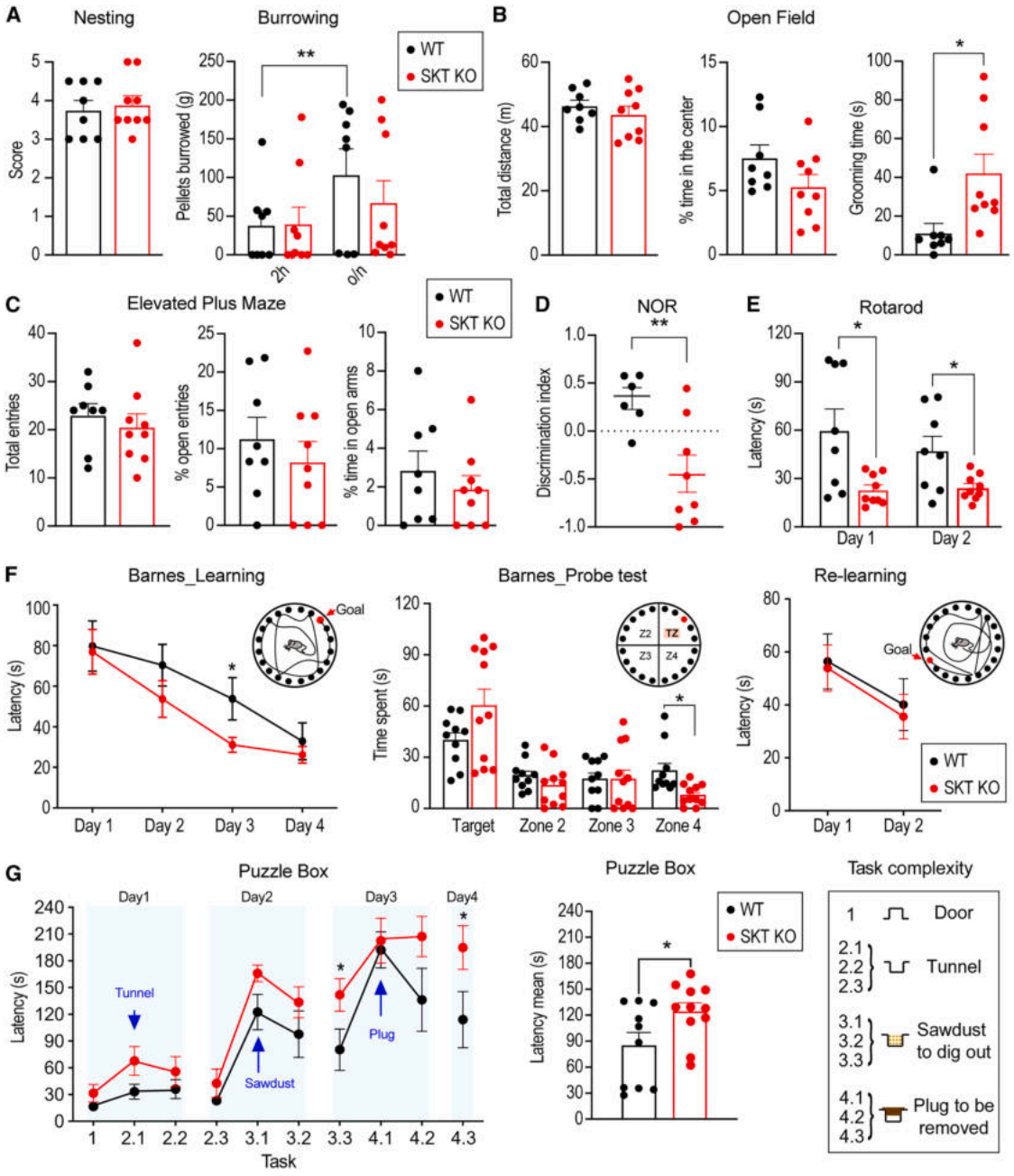

Figure 7. *SKT*-KO mice show alterations in many behavioral domains

A battery of behavioral tests was conducted to assess *SKT*-KO and WT control mouse phenotypes. The total number of animals is shown in the dotted plots. Error bars indicate SEM.

(A) Mice were tested for activities of daily living (ADL), in particular nesting and burrowing activities. Nesting: $p = 0.7$ by unpaired t test. Burrowing: $F(1,15) = 0.29$, $p = 0.6$ by two-way RM ANOVA. $^{**}p < 0.01$, 2 h vs. overnight (o/n) burrowing activity only for WT control (WT: $p = 0.002$; SKT-KO: $p = 0.12$) using Fisher's LSD test after two-way RM ANOVA.

(B) Evaluation of locomotor and exploratory activity in the OF test revealed no differences in overall distance traveled ($p = 0.4$) and in the percentage of time spent in the center ($p = 0.1$) but indicates increased time in grooming activity in *SKT*-KO mice ($p = 0.015$). $^{*}p < 0.05$ compared with WT control, using unpaired t test.

(C) All mice under study exhibited no change in anxious-like behavior in the EPM test (total entries: $p = 0.5$; % of entries in the open arms: $p = 0.4$ and % of time in the open arms: $p = 0.4$ by unpaired t test).

(D) Novel object discrimination index indicates that *SKT*-KO mice made fewer explorations of the novel object ($p = 0.008$), $^{**}p < 0.01$ compared with WT control, using unpaired t test.

(E) *SKT*-KO mice showed reduced latency to fall from the accelerating rotarod during the 2 days of testing. (Day1: $p = 0{,}01$; Day2: $p = 0.02$), $^{*}p < 0.05$ compared with WT control, using unpaired t test.

(legend continued on next page)

Altered synaptic functionality is an element underlying several neuropathologies ("synaptopathies"), especially those associated with neurodevelopment, such as ASD. Future investigations on *SKT*-KO mice should also incorporate specific tests designed to assess sociability.

Motor-related deficits may be a confounding element for the interpretation of cognitive tests. The observed reduction in performance in the PB could, at least in part, originate from frustration associated with motor difficulties rather than solely reflecting a lack of attention or cognitive abilities.

Finally, in this study, we focused only on male mice, given the well-known prevalence of ASD in males; thus, extending these investigations to female mice will be critical in future research to achieve a more comprehensive understanding.

RESOURCE AVAILABILITY

Lead contact

Requests for further information and resources should be directed to and will be fulfilled by the lead contact, Paola Defilippi (paola.defilippi@unito.it).

Materials availability

All reagents/materials generated in this study will be made available upon reasonable request. The request may require a completed materials transfer agreement.

Data and code availability

- The Python algorithm is available on Zenodo at https://doi.org/10.5281/zenodo.14230311.
- This paper does not report the original code.
- Any additional information required to reanalyze the data reported in this paper is available from the lead contact upon reasonable request.

ACKNOWLEDGMENTS

Dr. Carola Eva prematurely passed away in November 2023. The colleagues who had the privilege to collaborate with her dedicate this manuscript to her memory. The research leading to these results has received funding from Italian Ministry of University and Research (MUR), PRIN 2022 project number 2022WYAEWE, PI P.D., and PRIN 2022 project number 20228HRTJ2, PI E.C., and from AIRC under IG 2022 – ID 27353 project, PI P.D. This work was also supported by Fondazione CRT 2020.1798, RILO University of Torino (IG 11904, IG 15538), and Italian Ministry of Health (MSAL) (RF-2021-12371961) to P.D.; PNRR M4C2-Investimento 1.4–529 CN00000041 "Finanziato dall'Unione Europea-NextGenerationEU" to P.D.; and RILO University of Torino to I.B. This work was also supported by the Italian Ministry of University and Research (MUR) national project "Dipartimenti di Eccellenza 2023/27" awarded to the Department of Neuroscience "Rita Levi Montalcini" (University of Torino).

AUTHOR CONTRIBUTIONS

Conceptualization, I.B., E.T., and P.D.; cell biology experiments and data analysis, A. Morellato, M.D.G., C.A., V.B., A.A., B.B., O.T.B., V.S., F.N., G.D., R.O., G. Centonze, and D.N.; *in vivo* analyses, A. Morellato, C.A., A.A., M.D.G., B.B., A.G., M. Giusetto and A.R.; immunofluorescence analyses, A. Morellato, V.B., M.D.G., O.T.B., and M. Gai; electrophysiological analyses, A. Marcantoni, A. R., A.B., D.G., E.C., E.H., G. Chiantia, and V.C.; behavioral assays, P.M., C. E., A.L., and I.B.; writing – original draft and editing, A. Morellato, M.D.G., A. B., E.T., I.B., and P.D.; writing – review, all authors.

DECLARATION OF INTERESTS

The authors declare no competing interests.

STAR★METHODS

Detailed methods are provided in the online version of this paper and include the following:

- KEY RESOURCES TABLE
- EXPERIMENTAL MODEL AND SUBJECT DETAILS
  - Mouse model
  - Cell lines
  - Primary mouse hippocampal neurons cultures
  - Slice preparation for electrophysiology
- METHOD DETAILS
  - Anti-SKT antibody generation
  - Tissue extracts preparation
  - Crude synaptosomes and post-synapse preparation
  - Cell transfection
  - Plasmid constructs
  - Western blot and immunoprecipitation
  - BioID assay
  - Neurons cultures transfection
  - Immunofluorescence
  - Analysis of dendritic spines and fluorescence co-localization
  - Small GTPases activity assay
  - Mouse perfusion and staining
  - MEA recordings and analysis
  - Solutions and drugs for electrophysiology
  - Patch clamp
  - Behavioral tests
  - Activity of daily life
  - Nest building
  - Burrowing test
  - Open field test
  - Novel object recognition test
  - Elevated plus maze test
  - Rotarod test
  - Barnes maze
  - Puzzle Box test
  - Statistics for behavioral tests
- QUANTIFICATION AND STATISTICAL ANALYSIS

SUPPLEMENTAL INFORMATION

Supplemental information can be found online at https://doi.org/10.1016/j.celrep.2025.116206.

Received: May 24, 2024
Revised: July 17, 2025
Accepted: August 5, 2025
Published: September 1, 2025

(F) Barnes maze test. All mice under study exhibited normal learning and spatial reference memory performance. Learning: genotype $F(1,19) = 2.15$, $p = 0.16$; genotype-days $F(3,57) = 0.64$, $p = 0.6$; days $F(1.9, 37.21) = 14.21$, $p < 0.0001$. Probe: genotype $F(1,19) = 0.12$, $p = 0.73$; genotype-quadrants $F(3,57) = 2.9$, $p = 0.04$; quadrants $F(1.47,28.03) = 15.64$, $p = 0.0001$. Re-learning: genotype $F(1,19) = 0.09$, $p = 0.8$; genotype-days $F(1,19) = 0.03$, $p = 0.9$; days $F(1,19) = 7.6$, $p = 0.01$ by two-way RM ANOVA.*$p < 0.05$ ($p = 0.046$) at day 3, using unpaired t test.

(G) Puzzle-box test. *SKT*-KO mice showed increased latency to accomplish the different tasks during the days of testing. Two-way RM ANOVA revealed a significant effect of genotype ($F(1,19) = 4.96$, $p = 0.038$) and *$p < 0.05$ compared with WT control, using Gehan-Breslow-Wilcoxon survival test and Mann-Whitney test. In the center, the total latency is significantly different between WT and *SKT* KO mice ($p = 0.038$), *$p < 0.05$ by unpaired t test.

REFERENCES

1. Yuste, R., and Denk, W. (1995). Dendritic spines as basic functional units of neuronal integration. Nature *375*, 682–684. https://doi.org/10.1038/375682a0.
2. Lepeta, K., Lourenco, M.V., Schweitzer, B.C., Martino Adami, P.V., Banerjee, P., Catuara-Solarz, S., de La Fuente Revenga, M., Guillem, A.M., Haidar, M., Ijomone, O.M., et al. (2016). Synaptopathies: synaptic dysfunction in neurological disorders - A review from students to students. J. Neurochem. *138*, 785–805. https://doi.org/10.1111/jnc.13713.
3. Tumer, Z., Dye, T.J., Prada, C., White-Brown, A.M., MacKenzie, A., and Levy, A.M. (1993). DLG4-Related Synaptopathy. In GeneReviews((R)), M.P. Adam, J. Feldman, G.M. Mirzaa, R.A. Pagon, S.E. Wallace, L.J.H. Bean, K.W. Gripp, and A. Amemiya, eds. (University of Washington, Seattle).
4. Roy, M., Sorokina, O., Skene, N., Simonnet, C., Mazzo, F., Zwart, R., Sher, E., Smith, C., Armstrong, J.D., and Grant, S.G.N. (2018). Proteomic analysis of postsynaptic proteins in regions of the human neocortex. Nat. Neurosci. *21*, 130–138. https://doi.org/10.1038/s41593-017-0025-9.
5. Zhu, F., Cizeron, M., Qiu, Z., Benavides-Piccione, R., Kopanitsa, M.V., Skene, N.G., Koniaris, B., DeFelipe, J., Fransén, E., Komiyama, N.H., and Grant, S.G.N. (2018). Architecture of the Mouse Brain Synaptome. Neuron *99*, 781–799.e10. https://doi.org/10.1016/j.neuron.2018.07.007.
6. Sheng, M., and Kim, E. (2011). The postsynaptic organization of synapses. Cold Spring Harb. Perspect. Biol. *3*, a005678. https://doi.org/10.1101/cshperspect.a005678.
7. de Bartolomeis, A., Latte, G., Tomasetti, C., and Iasevoli, F. (2014). Glutamatergic postsynaptic density protein dysfunctions in synaptic plasticity and dendritic spines morphology: relevance to schizophrenia and other behavioral disorders pathophysiology, and implications for novel therapeutic approaches. Mol. Neurobiol. *49*, 484–511. https://doi.org/10.1007/s12035-013-8534-3.
8. Levy, A.M., Gomez-Puertas, P., and Tumer, Z. (2022). Neurodevelopmental Disorders Associated with PSD-95 and Its Interaction Partners. Int. J. Mol. Sci. *23*, 4390. https://doi.org/10.3390/ijms23084390.
9. Monteiro, P., and Feng, G. (2017). SHANK proteins: roles at the synapse and in autism spectrum disorder. Nat. Rev. Neurosci. *18*, 147–157. https://doi.org/10.1038/nrn.2016.183.
10. Repetto, D., Camera, P., Melani, R., Morello, N., Russo, I., Calcagno, E., Tomasoni, R., Bianchi, F., Berto, G., Giustetto, M., et al. (2014). p140Cap regulates memory and synaptic plasticity through Src-mediated and citron-N-mediated actin reorganization. J. Neurosci. *34*, 1542–1553. https://doi.org/10.1523/JNEUROSCI.2341-13.2014.
11. Alfieri, A., Sorokina, O., Adrait, A., Angelini, C., Russo, I., Morellato, A., Matteoli, M., Menna, E., Boeri Erba, E., McLean, C., et al. (2017). Synaptic Interactome Mining Reveals p140Cap as a New Hub for PSD Proteins Involved in Psychiatric and Neurological Disorders. Front. Mol. Neurosci. *10*, 212. https://doi.org/10.3389/fnmol.2017.00212.
12. Yao, M., Meng, M., Yang, X., Wang, S., Zhang, H., Zhang, F., Shi, L., Zhang, Y., Zhang, X., and Xu, Z. (2022). POSH regulates assembly of the NMDAR/PSD-95/Shank complex and synaptic function. Cell Rep. *39*, 110642. https://doi.org/10.1016/j.celrep.2022.110642.
13. Li, M.Y., Miao, W.Y., Wu, Q.Z., He, S.J., Yan, G., Yang, Y., Liu, J.J., Taketo, M.M., and Yu, X. (2017). A Critical Role of Presynaptic Cadherin/Catenin/p140Cap Complexes in Stabilizing Spines and Functional Synapses in the Neocortex. Neuron *94*, 1155–1172.e8. https://doi.org/10.1016/j.neuron.2017.05.022.
14. van Oostrum, M., Blok, T.M., Giandomenico, S.L., Tom Dieck, S., Tushev, G., Fürst, N., Langer, J.D., and Schuman, E.M. (2023). The proteomic landscape of synaptic diversity across brain regions and cell types. Cell *186*, 5411–5427.e23. https://doi.org/10.1016/j.cell.2023.09.028.
15. Karasugi, T., Semba, K., Hirose, Y., Kelempisioti, A., Nakajima, M., Miyake, A., Furuichi, T., Kawaguchi, Y., Mikami, Y., Chiba, K., et al. (2009). Association of the tag SNPs in the human SKT gene (KIAA1217) with lumbar disc herniation. J. Bone Miner. Res. *24*, 1537–1543. https://doi.org/10.1359/jbmr.090314.
16. Semba, K., Araki, K., Li, Z., Matsumoto, K.i., Suzuki, M., Nakagata, N., Takagi, K., Takeya, M., Yoshinobu, K., Araki, M., et al. (2006). A novel murine gene, Sickle tail, linked to the Danforth's short tail locus, is required for normal development of the intervertebral disc. Genetics *172*, 445–456. https://doi.org/10.1534/genetics.105.048934.
17. Al Dhaheri, N., Wu, N., Zhao, S., Wu, Z., Blank, R.D., Zhang, J., Raggio, C., Halanski, M., Shen, J., Noonan, K., et al. (2020). KIAA1217: A novel candidate gene associated with isolated and syndromic vertebral malformations. Am. J. Med. Genet. *182*, 1664–1672. https://doi.org/10.1002/ajmg.a.61607.
18. Suda, H., Lee, K.J., Semba, K., Kyushima, F., Ando, T., Araki, M., Araki, K., Inomata, Y., and Yamamura, K.i. (2011). The Skt gene, required for anorectal development, is a candidate for a molecular marker of the cloacal plate. Pediatr. Surg. Int. *27*, 269–273. https://doi.org/10.1007/s00383-010-2785-0.
19. Barik, A., Katuwawala, A., Hanson, J., Paliwal, K., Zhou, Y., and Kurgan, L. (2020). DEPICTER: Intrinsic Disorder and Disorder Function Prediction Server. J. Mol. Biol. *432*, 3379–3387. https://doi.org/10.1016/j.jmb.2019.12.030.
20. Kim, E., and Sheng, M. (2004). PDZ domain proteins of synapses. Nat. Rev. Neurosci. *5*, 771–781. https://doi.org/10.1038/nrn1517.
21. McGee, A.W., Dakoji, S.R., Olsen, O., Bredt, D.S., Lim, W.A., and Prehoda, K.E. (2001). Structure of the SH3-guanylate kinase module from PSD-95 suggests a mechanism for regulated assembly of MAGUK scaffolding proteins. Mol. Cell *8*, 1291–1301. https://doi.org/10.1016/s1097-2765(01)00411-7.
22. Varnaite, R., and MacNeill, S.A. (2016). Meet the neighbors: Mapping local protein interactomes by proximity-dependent labeling with BioID. Proteomics *16*, 2503–2518. https://doi.org/10.1002/pmic.201600123.
23. von Bohlen Und Halbach, O. (2009). Structure and function of dendritic spines within the hippocampus. Ann. Anat. *191*, 518–531. https://doi.org/10.1016/j.aanat.2009.08.006.
24. Porrero, C., Rubio-Garrido, P., Avendaño, C., and Clascá, F. (2010). Mapping of fluorescent protein-expressing neurons and axon pathways in adult and developing Thy1-eYFP-H transgenic mice. Brain Res. *1345*, 59–72. https://doi.org/10.1016/j.brainres.2010.05.061.
25. Penzes, P., and Rafalovich, I. (2012). Regulation of the actin cytoskeleton in dendritic spines. Adv. Exp. Med. Biol. *970*, 81–95. https://doi.org/10.1007/978-3-7091-0932-8_4.
26. Spence, E.F., and Soderling, S.H. (2015). Actin Out: Regulation of the Synaptic Cytoskeleton. J. Biol. Chem. *290*, 28613–28622. https://doi.org/10.1074/jbc.R115.655118.
27. Borovac, J., Bosch, M., and Okamoto, K. (2018). Regulation of actin dynamics during structural plasticity of dendritic spines: Signaling messengers and actin-binding proteins. Mol. Cell. Neurosci. *91*, 122–130. https://doi.org/10.1016/j.mcn.2018.07.001.
28. Oh, D., Han, S., Seo, J., Lee, J.R., Choi, J., Groffen, J., Kim, K., Cho, Y.S., Choi, H.S., Shin, H., et al. (2010). Regulation of synaptic Rac1 activity, long-term potentiation maintenance, and learning and memory by BCR and ABR Rac GTPase-activating proteins. J. Neurosci. *30*, 14134–14144. https://doi.org/10.1523/JNEUROSCI.1711-10.2010.
29. Salomaa, S.I., Miihkinen, M., Kremneva, E., Paatero, I., Lilja, J., Jacquemet, G., Vuorio, J., Antenucci, L., Kogan, K., Hassani Nia, F., et al. (2021). SHANK3 conformation regulates direct actin binding and crosstalk with Rap1 signaling. Curr. Biol. *31*, 4956–4970.e9. https://doi.org/10.1016/j.cub.2021.09.022.
30. Pontrello, C.G., and Ethell, I.M. (2009). Accelerators, Brakes, and Gears of Actin Dynamics in Dendritic Spines. Open Neurosci. J. *3*, 67–86. https://doi.org/10.2174/1874082000903020067.
31. Gavello, D., Rojo-Ruiz, J., Marcantoni, A., Franchino, C., Carbone, E., and Carabelli, V. (2012). Leptin counteracts the hypoxia-induced inhibition of

spontaneously firing hippocampal neurons: a microelectrode array study. PLoS One *7*, e41530. https://doi.org/10.1371/journal.pone.0041530.

32. Russo, I., Gavello, D., Menna, E., Vandael, D., Veglia, C., Morello, N., Corradini, I., Focchi, E., Alfieri, A., Angelini, C., et al. (2019). p140Cap Regulates GABAergic Synaptogenesis and Development of Hippocampal Inhibitory Circuits. Cereb. Cortex *29*, 91–105. https://doi.org/10.1093/cercor/bhx306.
33. Gavello, D., Calorio, C., Franchino, C., Cesano, F., Carabelli, V., Carbone, E., and Marcantoni, A. (2018). Early Alterations of Hippocampal Neuronal Firing Induced by Abeta42. Cereb. Cortex *28*, 433–446. https://doi.org/10.1093/cercor/bhw377.
34. Allio, A., Calorio, C., Franchino, C., Gavello, D., Carbone, E., and Marcantoni, A. (2015). Bud extracts from Tilia tomentosa Moench inhibit hippocampal neuronal firing through GABAA and benzodiazepine receptors activation. J. Ethnopharmacol. *172*, 288–296. https://doi.org/10.1016/j.jep.2015.06.016.
35. Hidisoglu, E., Chiantia, G., Franchino, C., Tomagra, G., Giustetto, M., Carbone, E., Carabelli, V., and Marcantoni, A. (2022). The ryanodine receptor-calstabin interaction stabilizer S107 protects hippocampal neurons from GABAergic synaptic alterations induced by Abeta42 oligomers. J. Physiol. *600*, 5295–5309. https://doi.org/10.1113/JP283537.
36. Chiantia, G., Comai, D., Hidisoglu, E., Gurgone, A., Franchino, C., Carabelli, V., Marcantoni, A., and Giustetto, M. (2025). Glyphosate impairs both structure and function of GABAergic synapses in hippocampal neurons. Neuropharmacology *262*, 110183. https://doi.org/10.1016/j.neuropharm.2024.110183.
37. Deacon, R.M.J. (2006). Burrowing in rodents: a sensitive method for detecting behavioral dysfunction. Nat. Protoc. *1*, 118–121. https://doi.org/10.1038/nprot.2006.19.
38. Bertocchi, I., Mele, P., Ferrero, G., Oberto, A., Carulli, D., and Eva, C. (2021). NPY-Y1 receptor signaling controls spatial learning and perineuronal net expression. Neuropharmacology *184*, 108425. https://doi.org/10.1016/j.neuropharm.2020.108425.
39. Longo, A., Fadda, M., Brasso, C., Mele, P., Palanza, P., Nanavaty, I., Bertocchi, I., Oberto, A., and Eva, C. (2018). Conditional inactivation of Npy1r gene in mice induces behavioural inflexibility and orbitofrontal cortex hyperactivity that are reversed by escitalopram. Neuropharmacology *133*, 12–22. https://doi.org/10.1016/j.neuropharm.2018.01.018.
40. Penzes, P., Cahill, M.E., Jones, K.A., VanLeeuwen, J.E., and Woolfrey, K.M. (2011). Dendritic spine pathology in neuropsychiatric disorders. Nat. Neurosci. *14*, 285–293. https://doi.org/10.1038/nn.2741.
41. Phillips, M., and Pozzo-Miller, L. (2015). Dendritic spine dysgenesis in autism related disorders. Neurosci. Lett. *601*, 30–40. https://doi.org/10.1016/j.neulet.2015.01.011.
42. Durand, C.M., Perroy, J., Loll, F., Perrais, D., Fagni, L., Bourgeron, T., Montcouquiol, M., and Sans, N. (2012). SHANK3 mutations identified in autism lead to modification of dendritic spine morphology via an actin-dependent mechanism. Mol. Psychiatry *17*, 71–84. https://doi.org/10.1038/mp.2011.57.
43. Grant, S.G.N. (2013). SnapShot: Organizational principles of the postsynaptic proteome. Neuron *80*, 534.e1. https://doi.org/10.1016/j.neuron.2013.10.014.
44. Sala, C., Vicidomini, C., Bigi, I., Mossa, A., and Verpelli, C. (2015). Shank synaptic scaffold proteins: keys to understanding the pathogenesis of autism and other synaptic disorders. J. Neurochem. *135*, 849–858. https://doi.org/10.1111/jnc.13232.
45. Faust, T.E., Gunner, G., and Schafer, D.P. (2021). Mechanisms governing activity-dependent synaptic pruning in the developing mammalian CNS. Nat. Rev. Neurosci. *22*, 657–673. https://doi.org/10.1038/s41583-021-00507-y.
46. Shi, Y., Pontrello, C.G., DeFea, K.A., Reichardt, L.F., and Ethell, I.M. (2009). Focal adhesion kinase acts downstream of EphB receptors to maintain mature dendritic spines by regulating cofilin activity. J. Neurosci. *29*, 8129–8142. https://doi.org/10.1523/JNEUROSCI.4681-08.2009.
47. Pontrello, C.G., Sun, M.Y., Lin, A., Fiacco, T.A., DeFea, K.A., and Ethell, I.M. (2012). Cofilin under control of beta-arrestin-2 in NMDA-dependent dendritic spine plasticity, long-term depression (LTD), and learning. Proc. Natl. Acad. Sci. USA *109*, E442–E451. https://doi.org/10.1073/pnas.1118803109.
48. Tomasoni, R., Repetto, D., Morini, R., Elia, C., Gardoni, F., Di Luca, M., Turco, E., Defilippi, P., and Matteoli, M. (2013). SNAP-25 regulates spine formation through postsynaptic binding to p140Cap. Nat. Commun. *4*, 2136. https://doi.org/10.1038/ncomms3136.
49. Angelini, C., Morellato, A., Alfieri, A., Pavinato, L., Cravero, T., Bianciotto, O.T., Salemme, V., Natalini, D., Centonze, G., Raspanti, A., et al. (2022). p140Cap regulates the composition and localization of the NMDAR complex in synaptic lipid rafts. J. Neurosci. *42*, 7183–7200. https://doi.org/10.1523/JNEUROSCI.1775-21.2022.
50. Salemme, V., Vedelago, M., Sarcinella, A., Moietta, F., Piccolantonio, A., Moiso, E., Centonze, G., Manco, M., Guala, A., Lamolinara, A., et al. (2023). p140Cap inhibits beta-Catenin in the breast cancer stem cell compartment instructing a protective anti-tumor immune response. Nat. Commun. *14*, 2350. https://doi.org/10.1038/s41467-023-37824-y.
51. Bolte, S., and Cordelières, F.P. (2006). A guided tour into subcellular colocalization analysis in light microscopy. J. Microsc. *224*, 213–232. https://doi.org/10.1111/j.1365-2818.2006.01706.x.
52. Del Pino, I., Tocco, C., Magrinelli, E., Marcantoni, A., Ferraguto, C., Tomagra, G., Bertacchi, M., Alfano, C., Leinekugel, X., Frick, A., and Studer, M. (2020). COUP-TFI/Nr2f1 Orchestrates Intrinsic Neuronal Activity during Development of the Somatosensory Cortex. Cereb. Cortex *30*, 5667–5685. https://doi.org/10.1093/cercor/bhaa137.
53. Feyder, M., Karlsson, R.M., Mathur, P., Lyman, M., Bock, R., Momenan, R., Munasinghe, J., Scattoni, M.L., Ihne, J., Camp, M., et al. (2010). Association of mouse Dlg4 (PSD-95) gene deletion and human DLG4 gene variation with phenotypes relevant to autism spectrum disorders and Williams' syndrome. Am. J. Psychiatry *167*, 1508–1517. https://doi.org/10.1176/appi.ajp.2010.10040484.
54. Dudchenko, P.A. (2004). An overview of the tasks used to test working memory in rodents. Neurosci. Biobehav. Rev. *28*, 699–709. https://doi.org/10.1016/j.neubiorev.2004.09.002.
55. Cirulli, E.T., Kasperaviciūte, D., Attix, D.K., Need, A.C., Ge, D., Gibson, G., and Goldstein, D.B. (2010). Common genetic variation and performance on standardized cognitive tests. Eur. J. Hum. Genet. *18*, 815–820. https://doi.org/10.1038/ejhg.2010.2.
56. Bauer, H.F., Delling, J.P., Bockmann, J., Boeckers, T.M., and Schön, M. (2022). Development of sex- and genotype-specific behavioral phenotypes in a Shank3 mouse model for neurodevelopmental disorders. Front. Behav. Neurosci. *16*, 1051175. https://doi.org/10.3389/fnbeh.2022.1051175.
57. Eltokhi, A., Bertocchi, I., Rozov, A., Jensen, V., Borchardt, T., Taylor, A., Proenca, C.C., Rawlins, J.N.P., Bannerman, D.M., and Sprengel, R. (2023). Distinct effects of AMPAR subunit depletion on spatial memory. iScience *26*, 108116. https://doi.org/10.1016/j.isci.2023.108116.
58. Sharan, S.K., Thomason, L.C., Kuznetsov, S.G., and Court, D.L. (2009). Recombineering: a homologous recombination-based method of genetic engineering. Nat. Protoc. *4*, 206–223. https://doi.org/10.1038/nprot.2008.227.
59. Uhrig, S., Vandael, D., Marcantoni, A., Dedic, N., Bilbao, A., Vogt, M.A., Hirth, N., Broccoli, L., Bernardi, R.E., Schönig, K., et al. (2017). Differential Roles for L-Type Calcium Channel Subtypes in Alcohol Dependence. Neuropsychopharmacology *42*, 1058–1069. https://doi.org/10.1038/npp.2016.266.
60. Marcantoni, A., Raymond, E.F., Carbone, E., and Marie, H. (2014). Firing properties of entorhinal cortex neurons and early alterations in an Alzheimer's disease transgenic model. Pflugers Arch. *466*, 1437–1450. https://doi.org/10.1007/s00424-013-1368-z.

61. Uhlen, M., Bandrowski, A., Carr, S., Edwards, A., Ellenberg, J., Lundberg, E., Rimm, D.L., Rodriguez, H., Hiltke, T., Snyder, M., and Yamamoto, T. (2016). A proposal for validation of antibodies. Nat. Methods *13*, 823–827. https://doi.org/10.1038/nmeth.3995.

62. Marcantoni, A., Chiantia, G., Tomagra, G., Hidisoglu, E., Franchino, C., Carabelli, V., and Carbone, E. (2023). Two firing modes and well-resolved Na(+), K(+), and Ca(2+) currents at the cell-microelectrode junction of spontaneously active rat chromaffin cell on MEAs. Pflugers Arch. *475*, 181–202. https://doi.org/10.1007/s00424-022-02761-0.

63. Siller, A., Hofer, N.T., Tomagra, G., Burkert, N., Hess, S., Benkert, J., Gaifullina, A., Spaich, D., Duda, J., Poetschke, C., et al. (2022). beta2-subunit alternative splicing stabilizes Cav2.3 Ca(2+) channel activity during continuous midbrain dopamine neuron-like activity. eLife *11*, e67464. https://doi.org/10.7554/eLife.67464.

64. Luvuno, M., Khathi, A., and Mabandla, M.V. (2020). The effects of exercise treatment on learning and memory ability, and cognitive performance in diet-induced prediabetes animals. Sci. Rep. *10*, 15048. https://doi.org/10.1038/s41598-020-72098-0.

STAR★METHODS

KEY RESOURCES TABLE

REAGENT or RESOURCE	SOURCE	IDENTIFIER
Antibodies		
Rabbit polyclonal anti-SKT	Antibody facility of the DBMSS (University of Torino)	N/A
Mouse monoclonal anti-p140Cap (clone 2A8)	Antibody facility of the DBMSS (University of Torino)	N/A
Rabbit polyclonal anti-GFP	Antibody facility of the DBMSS (University of Torino)	N/A
Mouse monoclonal anti-GFP (clone 2G8/C11)	Antibody facility of the DBMSS (University of Torino)	N/A
Mouse monoclonal anti-PSD-95 (clone 6G6-1C9)	Abcam, Cambridge, UK	Cat# ab2723; RRID:AB_303248)
Mouse monoclonal anti-panSHANK (clone N23B/49)	Sigma-Aldrich, St. Louis, MO, USA	Cat# MABN24; RRID:AB_11213314
Rabbit polyclonal anti-CAMKII-alfa	Cell Signaling, Danvers, MA, USA	Cat#3357; RRID:AB_2070308
Rabbit polyclonal anti-HOMER1	Thermo Fischer Scientific, Waltham, MA, USA	Cat#PA5-23023; RRID: AB_11154279
Mouse monoclonal anti-VGLUT1 (clone E9D2B)	Cell Signaling, Danvers, MA, USA	Cat#98199
Rabbit monoclonal anti-Beta-ACTIN (clone 13E5)	Cell Signaling, Danvers, MA, USA	Cat#4970; RRID:AB_2223172
Mouse monoclonal anti-Beta-CATENIN (clone 14)	BD Trasduction Laboratories, Franklin Lakes, NJ, USA	Cat#610153; RRID:AB_397554
Rabbit monoclonal anti-AXIN (C76H11)	Cell Signaling, Danvers, MA, USA	Cat#2087; RRID:AB_2274550
Mouse monoclonal anti-Alpha-TUBULIN (B512)	Sigma-Aldrich, St. Louis, MO, USA	Cat#T5168; RRID:AB_477579
Mouse monoclonal anti-HA-tag (2-2.2.14)	Thermo Fischer Scientific, Waltham, MA, USA	Cat# 26183; RRID:AB_2533052
Mouse monoclonal anti-RAC1 (clone N/A)	Cell Biolabs, San Diego, CA, USA	240106- Cat#STA-405
Mouse monoclonal anti-RHOA (clone N/A)	Cell Biolabs, San Diego, CA, USA	240302- Cat#STA-405
Rabbit monoclonal anti-COFILIN (clone D3F9)	Cell Signaling, Danvers, MA, USA	Cat#5175; RRID:AB_10622000
Rabbit monoclonal anti-Phospho-COFILIN (Ser3) (clone 77G2)	Cell Signaling, Danvers, MA, USA	Cat#3313; RRID:AB_2080597
Mouse monoclonal anti-IgGs (D-1)	Santa Cruz Biotechnology, Dallas, TX, USA	Cat#sc-515946; RRID:AB_3699201
Recombinant Guinea pig anti-VGAT	SYSY antibodies, Goettingen, DE	Cat#131308; RRID:AB_2832243
Anti-Rabbit IgG (whole molecule)–Peroxidase antibody produced in goat	Sigma-Aldrich, St. Louis, MO, USA	Cat#A6154; RRID:AB_258284
Anti-Mouse IgG (whole molecule)–Peroxidase antibody produced in goat	Sigma-Aldrich, St. Louis, MO, USA	Cat#A4416; RRID:AB_258167
Chicken polyclonal anti-MAP2	Abcam, Cambridge, UK	Cat#ab5392; RRID:AB_2138153
Mouse monoclonal anti-Myc tag (9B11)	Cell Signaling, Danvers, MA, USA	Cat#2276; RRID:AB_331783

(*Continued on next page*)

Continued

REAGENT or RESOURCE	SOURCE	IDENTIFIER
Rabbit polyclonal anti-GFAP	Agilent Technologies, Santa Clara, CA, USA	Cat#Z0334; RRID:AB_10013382
Chicken polyclonal anti-GFP	Abcam, Cambridge, UK	Cat#ab13970; RRID:AB_300798
Goat anti-Guinea Pig IgG (H+L) Highly Cross-Adsorbed Secondary Antibody, Alexa Fluor™ 568	Thermo Fischer Scientific, Waltham, MA, USA	Cat#A-11075; RRID:AB_2534119
Goat anti-Rabbit IgG (H+L) Cross-Adsorbed Secondary Antibody, Alexa Fluor™ 488	Thermo Fischer Scientific, Waltham, MA, USA	Cat#A-11008; RRID:AB_143165
Goat anti-Mouse IgG (H+L) Cross-Adsorbed Secondary Antibody, Alexa Fluor™ 488	Thermo Fischer Scientific, Waltham, MA, USA	Cat#A-11001; RRID:AB_2534069
Goat anti-Mouse IgG (H+L) Cross-Adsorbed Secondary Antibody, Alexa Fluor™ 568	Thermo Fischer Scientific, Waltham, MA, USA	Cat#A-11004; RRID:AB_2534072
Goat anti-Rabbit IgG (H+L) Highly Cross-Adsorbed Secondary Antibody, Alexa Fluor™ 568	Thermo Fischer Scientific, Waltham, MA, USA	Cat#A-11036; RRID:AB_10563566
Goat anti-Mouse IgG (H+L) Cross-Adsorbed Secondary Antibody, Alexa Fluor™ 405	Thermo Fischer Scientific, Waltham, MA, USA	Cat#A-31553; RRID:AB_221604
Goat anti-Rabbit IgG (H+L) Cross-Adsorbed Secondary Antibody, Alexa Fluor™ 405	Thermo Fischer Scientific, Waltham, MA, USA	Cat#A-31556; RRID:AB_221605
Goat anti-Chicken IgY (H+L) Cross-Adsorbed Secondary Antibody, Alexa Fluor™ Plus 647	Thermo Fischer Scientific, Waltham, MA, USA	Cat#A32933; RRID:AB_2762845
Goat anti-Chicken IgY (H+L) Secondary Antibody, Alexa Fluor™ 488	Thermo Fischer Scientific, Waltham, MA, USA	Cat#A-11039; RRID:AB_2534096
Biological samples		
Mouse brain tissue (C57BL/6J (Mus musculus))	Animal facility of the DBMSS (University of Torino)	N/D
Primary mouse hippocampal neurons cultures	This paper	N/D
Mouse brain slices	Histology facility of the DBMSS (University of Torino)	N/D
Primary mouse astrocytes cultures	University of Torino	N/D
Chemicals, peptides, and recombinant proteins		
NaCl (sodium chloride)	Sigma-Aldrich, St. Louis, MO, USA	S9888
Trizma® base	Sigma-Aldrich, St. Louis, MO, USA	T1503
Glycerol	Sigma-Aldrich, St. Louis, MO, USA	G7893
NP-40 Surfact-Amps™ Detergent Solution	Thermo Fischer Scientific, Waltham, MA, USA	Cat#85124
MgCl2 hexahydrate (magnesium chloride)	Sigma-Aldrich, St. Louis, MO, USA	M2393
cOmplete™ Protease Inhibitor Cocktail	Sigma-Aldrich, St. Louis, MO, USA	11697498001
Bio-Rad Protein Assay Dye Reagent Concentrate	BioRad, Hercules, CA, USA	Cat#5000006
HEPES (1M)	Thermo Fischer Scientific, Waltham, MA, USA	Cat#15630056
Sucrose	Sigma-Aldrich, St. Louis, MO, USA	S0389

(*Continued on next page*)

Continued

REAGENT or RESOURCE	SOURCE	IDENTIFIER
EGTA (Ethylene-bis (oxyethylenenitrilo)tetraacetic acid)	Sigma-Aldrich, St. Louis, MO, USA	E3889-10G
Triton™ X-100	Sigma-Aldrich, St. Louis, MO, USA	T8787-50ML
DMEM, high glucose, GlutaMAX™ Supplement, pyruvate	Thermo Fischer Scientific, Waltham, MA, USA	Cat#10569010
Fetal Bovine Serum (FBS), Premium	Thermo Fischer Scientific, Waltham, MA, USA	Cat#A5670701
Penicillin-Streptomycin	Thermo Fischer Scientific, Waltham, MA, USA	Cat#15140122
Lipofectamine™ LTX Reagent with PLUS™ Reagent	Thermo Fischer Scientific, Waltham, MA, USA	Cat#15338100
Dynabeads™ Protein G for Immunoprecipitation	Thermo Fischer Scientific, Waltham, MA, USA	Cat#10004D
PBS (10X), pH 7.4	Thermo Fischer Scientific, Waltham, MA, USA	Cat#70011044
Tween 20, 100% Nonionic Detergent	BioRad, Hercules, CA, USA	Cat#1706531
2x Laemmli Sample Buffer	BioRad, Hercules, CA, USA	Cat#1610737
D-Biotin	Thermo Fischer Scientific, Waltham, MA, USA	Cat#B20656
EDTA (Ethylenediaminetetraacetic acid)	Sigma-Aldrich, St. Louis, MO, USA	E9884-100G
Sodium deoxycholate	Sigma-Aldrich, St. Louis, MO, USA	30970-25G
Pierce™ Streptavidin Agarose	Thermo Fischer Scientific, Waltham, MA, USA	Cat#20353
SDS (Sodium dodecyl sulfate)	Sigma-Aldrich, St. Louis, MO, USA	L3771-25G
Poly-L-lysine hydrobromide	Sigma-Aldrich, St. Louis, MO, USA	P1399-25MG
Neurobasal™ Medium	Thermo Fischer Scientific, Waltham, MA, USA	Cat#21103049
B-27™ Plus Supplement (50X)	Thermo Fischer Scientific, Waltham, MA, USA	Cat#A3582801
NeuroMag Transfection Reagent	OzBiosciences, San Diego, CA, USA	Cat#NM50500
PFA (Paraformaldehyde)	Sigma-Aldrich, St. Louis, MO, USA	158127-5G
BSA (Bovine Serum Albumin)	Sigma-Aldrich, St. Louis, MO, USA	A8806-1G
Goat Serum, New Zealand origin	Thermo Fischer Scientific, Waltham, MA, USA	Cat#16210064
Donkey Serum	Sigma-Aldrich, St. Louis, MO, USA	S30-100ML
KCl (potassium chloride)	Sigma-Aldrich, St. Louis, MO, USA	P9541-500G
NaH_2PO_4 (Sodium phosphate monobasic)	Sigma-Aldrich, St. Louis, MO, USA	S3139-250G
$MgSO_4$ (Magnesium sulfate)	Sigma-Aldrich, St. Louis, MO, USA	M2643-500G
$CaCl_2$ (Calcium chloride)	Sigma-Aldrich, St. Louis, MO, USA	C5670-100G
$NaHCO_3$ (Sodium bicarbonate)	Sigma-Aldrich, St. Louis, MO, USA	S5761-500G
D-(+)-Glucose	Sigma-Aldrich, St. Louis, MO, USA	G7021-100G
D-AP5 (D(−)-2-Amino-5-phosphonopentanoic acid)	Sigma-Aldrich, St. Louis, MO, USA	A8054-1MG
Picrotoxin	Sigma-Aldrich, St. Louis, MO, USA	P1675-1G
CGP 55845 hydrochloride	Tocris (Bio-Techne SRL), Milano, IT	Cat#1248
Gluconic acid (K-gluconate)	Sigma-Aldrich, St. Louis, MO, USA	8220571000
MG-ATP (Adenosine 5′-triphosphate magnesium salt)	Sigma-Aldrich, St. Louis, MO, USA	A9187-100MG

(*Continued on next page*)

Continued

REAGENT or RESOURCE	SOURCE	IDENTIFIER
Tris-GTP (Guanosine 5′-triphosphate tris salt)	Sigma-Aldrich, St. Louis, MO, USA	G9002-10MG
TTX (Tetrodotoxin)	Tocris (Bio-Techne SRL), Milano, IT	Cat#1078
ATP-Tris (ATP Solution, Tris buffered)	Thermo Fischer Scientific, Waltham, MA, USA	Cat#R1441
QX-314 bromide (*N*-(2,6-Dimethylphenylcarbamoylmethyl) triethylammonium bromide)	Tocris (Bio-Techne SRL), Milano, IT	Cat#1014
GlutaMAX™ Supplement	Thermo Fischer Scientific, Waltham, MA, USA	Cat# 35050061
Rompun (Xilazina Cloridrato)	Elanco Italia SPA, Sesto Fiorentino, IT	Cat#100390018
Zoletil (Zolazepam + Tiletamina)	Virbac SRL, Milano, IT	Cat#101580025
DAPI (4′,6-Diamidino-2-phenylindole dihydrochloride, 2-(4-Amidinophenyl)-6-indolecarbamidine dihydrochloride)	Sigma-Aldrich, St. Louis, MO, USA	D9542-5MG
Critical commercial assays		
RhoA / Rac1 / Cdc42 Activation Assay Combo Biochem Kit (bead pull-down format)	Cyroskeleton, Inc., Denver, CO, USA	Cat#BK030
Deposited data		
Python algorithm	This paper	Zenodo: https://doi.org/10.5281/zenodo.14230311
Experimental models: Cell lines		
293T	ATCC, Manassas, VA, USA	CRL-3216
COS-7	ATCC, Manassas, VA, USA	CRL-1651
Experimental models: Organisms/strains		
Mouse: SKT knock-out (Mus musculus, (C57BL/6J))	This paper	N/D
Mouse: Tg(Thy1-EGFP)MJrs/J (Mus musculus, (C57BL/6J)) Strain #007788	The Jackson Laboratory, Bar Harbor, ME, USA	RRID:IMSR_JAX:007788
Oligonucleotides		
SKT fragment 1-320 Fw: CCGCTCG AGCACCATGGAAGAAAATGAAAG CCAG	This paper	N/D
SKT fragment 1-320 Rev: GCCGGT ACCTGAGAACCCCCAGAGATCTT TCTTT	This paper	N/D
SKT fragment 321-640 Fw: CCACT CGAGTACCATGGCACATTCCATG CCCCCCTCC	This paper	N/D
SKT fragment 321-640 Rev: GGGGT ACCTTGAGGTGCCCACAGGTGGA GGCTG	This paper	N/D
SKT fragment 641-823 Fw: CCGCT CGAGAACCATGGTAGCCATCCAC ATGAGC	This paper	N/D
SKT fragment 641-823 Rev: GGG GTACCCATCAGTGACATGTCTC CGCAG	This paper	N/D
hSyn Fw: CTGATTAATCACGCGTG TGTCTAGACTGCAGAGGG	This paper	N/D

(*Continued on next page*)

Continued

REAGENT or RESOURCE	SOURCE	IDENTIFIER
hSyn Rev: TTTACCGGTGCTAGCG GATCCGGTACCTTC	This paper	N/D
SKT N-terminal 1-187 fragment Fw: CCGCTCGAGGGCTCTGAAGAAAA TGAAAGCCAG	This paper	N/D
SKT N-terminal 1-187 fragment Rev: GCCGGTACCTGAGAACCCCCAG AGATCTTTCTTT	This paper	N/D
SKT C-terminal 1707-1943 fragment Fw: ACATAGCCCAAGAGGCCTCT CCCCGA	This paper	N/D
SKT C-terminal 1707-1943 Rev: CG CGAATTCAAGCTTAGAACCAGAG GTTTCTTTTGCTGT	This paper	N/D
N-terminal PSD-95 fragment (1-397) Fw: GGATCCTCATGGACTGTCTCT GATA	This paper	N/D
N-terminal PSD-95 fragment (1-397) Rev: AAGCTTTCATTTATACTGAGC GATGATCGTGAC	This paper	N/D
C-terminal PSD-95 fragment (430-724) Fw: GGATCCTCAACCCCAA GAGGGGCTTCTAC	This paper	N/D
C-terminal PSD-95 fragment (430-724) Rev: AAGCTTTCAGAGTCTC TCTCGGGCTGGGAC	This paper	N/D
Recombinant DNA		
KIAA1217(SKT)-pSPORT1	from the German Science Center for Genome Research RZPD	ID:IRAVp698B0149D6
KIAA1217(SKT)-pcDNA3.1 Myc-His(-) A	This paper	N/D
KIAA1217(SKT)-peGFP C1	This paper	N/D
KIAA1217(SKT)-pmRFP-C1	This paper	N/D
pAAV-hSyn-mCherry	Addgene, Watertown, MA, USA	Cat#114472
hSyn::GFP	This paper	N/D
hSyn::GFP-SKT	This paper	N/D
MCS-BirA(R118G)-HA	from Professor Thilo Kähne, Otto-Von-Guericke, University of Magdeburg, DE	N/D
pDNA3.1 MycBioID(R118G)	from Professor Thilo Kähne, Otto-Von-Guericke, University of Magdeburg, DE	N/D
Myc-BirA-SKT	This paper	N/D
SKT-BirA-HA	This paper	N/D
Rat GFP-(Myc)-PSD95	from Professor M. Matteoli, CNR, University of Milano, IT	N/D
pCMV2-PSD-95-flag	from Professor M. Matteoli, CNR, University of Milano, IT	N/D
PSD-95(1-397) peGFP-C2	This paper	N/D
PSD-95(430-724) peGFP-C2	This paper	N/D
Mouse HA-SHANK1	from Professor M. Giustetto, Neuroscience Department, University of Torino, IT	N/D

(*Continued on next page*)

Continued

REAGENT or RESOURCE	SOURCE	IDENTIFIER
Mouse HA-SHANK3	from Professor C. Sala, CNR, University of Milano, IT	N/D
GFP-C1-CAMKIIbeta	Addgene, Watertown, MA, USA	Cat#21227
GFP-C1-CAMKIIalpha	Addgene, Watertown, MA, USA	Cat#21226
Software and algorithms		
GraphPad Prism v9.0 and v10.4	GraphPad Software, San Diego, CA, USA	https://www.graphpad.com/
ImageJ software	Fiji ImageJ software, Rasband, W.S., U.S. National Institutes of Health, Bethesda, MD, USA	https://imagej.net/ij/
Neuroexplorer software	Nex Technologies, Littleton, MA, USA	https://www.neuroexplorer.com/
pCLAMP™ 10 software	Axon Instruments, Molecular Devices, Sunnyvale, CA, USA	https://it.moleculardevices.com/
Digidata 1440A acquisition interface	Molecular Devices, Sunnyvale, CA, USA	https://it.moleculardevices.com/
Minianalysis program	Synaptosoft, Leonia, NJ, USA	https://www.synaptosoft.com/
Clampfit software	Axon Instruments, Molecular Devices, Sunnyvale, CA, USA	https://it.moleculardevices.com/
Nikon NIS-Elements	Nikon Instruments Inc., Melville, NY, USA	https://www.microscope.healthcare.nikon.com/
EthoVision XT video track system, v17.5	Noldus Information Technology, Leesburg, VA, USA	https://noldus.com/
Microsoft Excel	Microsoft Corporation, Redmond, WA, USA	https://www.microsoft.com/
Python algorithm	This paper	Zenodo: https://doi.org/10.5281/zenodo.14230311
Other		
Mini-PROTEAN® TGX™ Precast Protein Gels, 10-well	BioRad, Hercules, CA, USA	Cat#4561084
Mini-PROTEAN® TGX™ Precast Protein Gels, 12-well	BioRad, Hercules, CA, USA	Cat#4561085
Mini-PROTEAN® TGX™ Precast Protein Gels, 15-well	BioRad, Hercules, CA, USA	Cat#4561086
Mowiol® 4-88	Sigma-Aldrich, St. Louis, MO, USA	81381-50G
ProLong™ Gold Antifade Mountant	Thermo Fischer Scientific, Waltham, MA, USA	Cat#P10144

EXPERIMENTAL MODEL AND SUBJECT DETAILS

Mouse model

To generate *SKT* KO mice, a neomycin-resistance cassette was cloned into the exon 7 using the recombineering technique[58], and the obtained construct was transfected by electroporation in 129Sv mouse ES cells. Four clones carrying the targeted allele were identified by Southern blotting and 1 of them injected into C57BL/6J mouse blastocysts. Chimeras were used to obtain heterozygous mice carrying the *SKT* $^{-/-}$ allele. After 10 generation of backcross with C57BL/6J*SKT* heterozygous mice we obtained the *SKT* $^{+/-}$ in the C57BL/6J strain.

The animals were maintained in a C57BL/6J genetic background and used as described in the following paragraphs. Mice harboring the *Thy1-GFP* transgene (The Jackson Laboratory, Bar Harbor, ME, USA) with enhanced green fluorescent protein (EGFP) expression under the control of a modified *Thy1* promoter region (containing the sequences required for neuronal expression but lacking the sequences required for expression in non-neural cells). Hemizygous *Thy1-GFP* mice derived from founder line M (*Thy1-GFP-M* or *Thy1-GFPM*) express EGFP in sparse subsets of neurons.

To generate *Thy1::GFP SKT* Knock-out (KO) mice and the relative wild-type (WT) controls, *SKT* KO females were bred with *Thy1::GFP* male. The *SKT* heterozygous *Thy1::GFP* were inbred to obtain the *SKT* KO and WT *Thy1::GFP* that were used for the

experiments. Our crosses did not generate *Thy1-GFP* homozygous mice. For all the following experiments adult male mice were used. All animals were maintained according to institutional animal welfare guidelines and legislation, approved by the local Animal Ethics Committee and the Ministry of Health. All experiments were approved and performed in accordance with the Italian law (authorization D.M. n°279/95B 27/11/1995) and dispositions of "D.L. n°116, 27/1/1992 concerning animal use and protection in scientific research".

Cell lines

Human HEK293T cells and COS-7 cells were obtained from the American Type Culture Collection (ATCC, Manassas, VA, USA). These cell lines were not authenticated. Both lines were tested for mycoplasma contamination routinely. Cells were cultured in DMEM + GlutaMAX supplement medium (Thermo Fisher Scientific, Waltham, MA, USA) supplemented with 10% heat-inactivated Fetal Bovine Serum (FBS) (Thermo Fisher Scientific, Waltham, MA, USA) and 1% Penicillin/Streptomycin (Thermo Fisher Scientific, Waltham, MA, USA).

Primary mouse hippocampal neurons cultures

Hippocampal neurons were isolated from E18.5 embryos derived from breeding of *SKT* heterozygous mice as described in Repetto et al., 2014[10]. The dissociated cells were plated onto 20 mm glass coverslips coated with poly-L lysine (Sigma-Aldrich, St. Louis, MO, USA) at the density of $1.2x10^5$ cells/coverslip and maintained in Neurobasal (Thermo Fisher Scientific, Waltham, MA, USA) supplemented with 2% B27 (Thermo Fisher Scientific, Waltham, MA, USA), 1% Penicillin/Streptomycin (Thermo Fisher Scientific, Waltham, MA, USA) and 1% GlutaMAX (Thermo Fisher Scientific, Waltham, MA, USA).

Slice preparation for electrophysiology

Male 3-month-old mice were sacrificed by cervical dislocation for acute brain slices. Slices preparation has been performed as previously described in Uhrig et al., 2017[59] and Marcantoni et al., 2014[60]. Hippocampal slices were kept at room temperature for at least 30 min before recording.

METHOD DETAILS

Anti-SKT antibody generation

Specific rabbit polyclonal antibodies against SKT were produced at the antibody facility of the DBMSS (University of Torino) by immunizing rabbits against a chimeric protein obtained by fusing pMAL with the sequence coding for a SKT peptide spanning from aa 816 to aa 1096 (see isoform coded by the transcript ID ENSMUST00000114627.8). The rabbit serum was purified of the antibodies against pMAL by a chromatography column. To validate SKT antibody, we followed some of the guidelines from Uhlen et al., 2016[61] that emphasize the importance of testing antibodies against overexpressed or purified proteins, but also of corroborating results with genetic controls, such as knockout (KO) models where the target protein's gene is deleted. In this work we used both approaches by analyzing either transfected HEK293 cells (Figure S1A), and tissue extracts from 3-month-old WT and *SKT* KO mice (Figure S1B). The molecular weight of the bands detected using the SKT antibody in Figure S1B matches the predicted molecular weight of the protein products deriving from the mouse *SKT* gene as reported in the Ensemble site as putative splicing isoforms: https://www.ensembl.org/Mus_musculus/Gene/Summary?db=core;g=ENSMUSG00000036617;r=2:19914591-20815524 (Figure S1C).

Tissue extracts preparation

Tissues from male 3-month-old mice were surgically removed and immediately frozen in liquid nitrogen, pounded and homogenized with Turax (5 strokes of 30 sec each) in ice-cold lysis buffer (150 mM NaCl, 50 mM Tris pH=7, 5% Glycerol, 1% NP-40, 1 mM MgCl2, 1X Roche protease inhibitors), followed by centrifugation (4°C, 16000 g, 45 min). The supernatant was collected and protein concentration was determined using the Bio-Rad protein assay method (BioRad, Hercules, CA, USA).

Crude synaptosomes and post-synapse preparation

Male, 3-month-old WT and *SKT* KO littermates were used for synaptosomes preparations from the telencephalon. Animals were sacrificed by cervical dislocation. The tissue was homogenized with a Dounce glass homogenizer and glass pestle in 8 mL ice-cold synaptosome buffer (4 mM Hepes pH=7.3, 320 mM sucrose, 1 mM EGTA, 1X Roche protease inhibitors). The homogenate was centrifuged at 1000 g for 10 min at 4°C. After discarding the nuclear pellet (P1), the supernatant (S1) was centrifuged at 12500 g for 20 min at 4°C to obtain a pellet (P2) containing Crude Synaptosome Fraction. A part of P2 was resuspended in the previously described synaptosome buffer supplemented with 1% Triton and 25 mM Hepes and ultracentrifuged at 100000 g for 1 hour to separate the supernatant Triton Soluble Fraction (TSF) and the Triton Insoluble Fraction (TIF) pellet. To purify the post synapse membrane, the remaining part of pellet P2 was resuspended in an hypoosmotic solution (to induce osmotic shock) and gently mixed for 30 minutes. Subsequently, the sample was centrifuged for 2 hours at 25000 g to obtain the S3 fraction (with synaptic vesicles) and the P3 pellet (containing the minority of presynaptic membranes). Finally, the S3 fraction was ultracentrifuged at 165000 g for 2 hours to isolate the majority of presynaptic vesicle membranes as the P4 pellet. The final pellets were resuspended in ice-cold lysis buffer (150 mM NaCl, 50 mM Tris pH=7, 5% Glycerol, 1% NP-40, 1 mM $MgCl_2$, 1X Roche protease inhibitors).

Cell transfection

HEK293T cells were transfected by calcium phosphate precipitation as previously described in Angelini, Morellato et al., 2022[49]. COS-7 cells were transfected with Lipofectamine LTX (Thermo Fischer Scientific, Waltham, MA, USA) as previously described in Angelini, Morellato et al., 2022[49]. Cell extracts were prepared with cold Lysis Buffer (150 mM NaCl, 50 mM Tris pH=7, 5% Glycerol, 1% NP-40, 1 mM $MgCl_2$, 1X Roche protease inhibitors), followed by centrifugation (4°C, 16000 g, 45 min). The supernatant was collected and protein concentration was determined using the Bio-Rad protein assay method (BioRad, Hercules, CA, USA).

Plasmid constructs

The human KIAA1217 (SKT) cDNA, in the pSPORT1 vector, was purchased from the German Science Center for Genome Research RZPD, ID:IRAVp698B0149D6 (alias DKFZP761L0424, GenBank accession n° AL833280.1) and then cloned into pcDNA3.1 Myc-His (-) A in frame with the Myc-His tag using the restriction enzymes KpnI and HindIII. SKT was then cloned into the peGFP-C1 and pmRFP-C1 vectors in frame with GFP and RFP, respectively, using the restriction enzymes XhoI and HindIII. The different cDNA fragments of SKT were obtained by PCR amplification adding unique restriction sites to clone in frame in peGFP-C2 and in pcDNA3.1 Myc-His (-) C vectors. The following primers were used:

SKT fragment 1-320 forward: CCGCTCGAGCACCATGGAAGAAAATGAAAGCCAG
SKT fragment 1-320 reverse: GCCGGTACCTGAGAACCCCCAGAGATCTTTCTTT
SKT fragment 321-640 forward: CCACTCGAGTACCATGGCACATTCCATGCCCCCCTCC
SKT fragment 321-640 reverse: GGGGTACCTTGAGGTGCCCACAGGTGGAGGCTG
SKT fragment 641-823 forward: CCGCTCGAGAACCATGGTAGCCATCCACATGAGC
SKT fragment 641-823 reverse: GGGGTACCCATCAGTGACATGTCTCCGCAG

The *Syn::*GFP-SKT plasmid was generated replacing the CMV promoter of pEGFP-SKT with the *Syn* promoter obtained by amplification using as template pAAV-hSyn-mCherry (Addgene, Watertown, MA, USA; Cat#114472). For the amplification were used the following primers:

*Syn::*GFP-SKT forward: CTGATTAATCACGCGTGTGTCTAGACTGCAGAGGG
*Syn::*GFP-SKT reverse: TTTACCGGTGCTAGCGGATCCGGTACCTTC

The amplified Syn promoter was cloned in pEGFP-SKT cut with restriction enzymes AseI and NheI. The same strategy was used to generate *Syn::GFP*. The MCS-BirA(R118G)-HA and pcDNA3.1 MycBioID (R118G) plasmids were a gift from Professor Thilo Kähne (Otto-Von-Guericke, University of Magdeburg). To generate the Myc-BirA-SKT construct, we used pcDNA3.1 MycBioID (R118G) plasmid (with BirA* located at the N-terminal end of SKT). The N-terminal SKT fragment (aa: 2-187) was generated by PCR using the following primers:

SKT N-terminal fragment 2-187 forward: CCGCTCGAGGGCTCTGAAGAAAATGAAAGCCAG
SKT N-terminal fragment 2-187 reverse GCCGGTACCTGAGAACCCCCAGAGATCTTTCTTT

The PCR product was cut with the restriction enzymes Xho and BglII. The fragment 188-1943 was obtained by digestion with the restriction enzymes BglII and HindIII of the SKT cDNA. The two fragments were cloned in MycBioID(R118G) cut with restriction enzymes XhoI and HindIII to generate the final construct Myc-BirA-hSKT. To generate the SKT-BirA-HA constructs, we used MCS-BirA (R118G)-HA plasmid (with BirA* located at the C-terminal end of SKT). The C-terminal SKT fragment (aa: 1707-1943) was generated by PCR with the following primers:

SKT C-terminal fragment 1707-1943 forward: ACATAGCCCAAGAGGCCTCTCCCCGA
SKT C-terminal fragment 1707-1943 reverse: CGCGAATTCAAGCTTAGAACCAGAGGTTTCTTTTGCTGT

The generated PCR product was cut with restriction enzymes BglI and EcoRI. To obtain the SKT fragment (aa:2-1706) NheI and BglI restriction enzymes were used to cut cDNA SKT; MCS-BirA(R118G)-HA was cut with NheI and EcoRI restriction enzymes to generate the final construct SKT-BirA-HA. Rat GFP-Myc-PSD-95 was a generous gift from Prof. M. Matteoli (CNR, University of Milano). We generate PSD-95 specific sub-domains by gene synthesis and molecular cloning approach using pCMV2-PSD95-flag as a template. PSD-95 fragments (aa: 1-397; aa: 430-724) were generated by PCR with the following primers:

PSD-95 fragment 1-397 forward: GGATCCTCATGGACTGTCTCTGATA
PSD-95 fragment 1-397 reverse: AAGCTTTCATTTATACTGAGCGATGATCGTGAC
PSD-95 fragment 430-724 forward: GGATCCTCAACCCCAAGAGGGGCTTCTAC
PSD-95 fragment 430-724 reverse: AAGCTTTCAGAGTCTCTCTCGGGCTGGGAC

The amplified DNAs were cut with the following restriction enzymes: BamHI and HindIII for PSD95 (aa: 1-397); XbaI and HindIII for PSD-95 (aa: 430-724). DNA fragments were then cloned in the peGFP-C2 vector cut with an appropriate couple of restriction enzymes. Mouse HA-SHANK1 and mouse HA-SHANK3 were kindly gifted by Prof. Giustetto and Prof. Sala (Neuroscience Department, University of Torino and CNR, University of Milan, respectively). The plasmids GFP-C1-CAMKIIbeta and GFP-C1-CAMKIIalfa were from Addgene, Watertown, MA, USA (Cat#21227 and Cat#21226 respectively).

Western blot and immunoprecipitation

For protein analysis SDS-PAGE was performed with Mini-PROTEAN® TGX™ Precast Protein Gels (BioRad, Hercules, CA, USA) gradient 4–15%, (10, 12 or 15 well) and WB as previously described in Angelini, Morellato et al., 2022[49]. For immunoprecipitation, 7 μl of Dynabeads™ Protein G 30 mg/mL (Thermo Fischer Scientific, Waltham, MA, USA) were initially washed using PBS, 0.05% Tween

and incubated with 1 μg of selected antibody diluted in the same buffer for 10 min at RT under gentle rotation. Antibody-coupled Dynabeads were then washed twice and incubated with 1 mg protein extract for 2 h at 4°C under gentle rotation. Beads were washed five times with cold Lysis Buffer (150 mM NaCl, 50 mM Tris pH=7, 5% Glycerol, 1% NP-40, 1 mM $MgCl_2$, 1X Roche protease inhibitors), then resuspended in a reducing buffer (2x Laemmli Sample Buffer; BioRad, Hercules, CA, USA) and incubated at 95°C for 10 min.

BioID assay

HEK293T cells were transiently transfected by calcium phosphate precipitation, as described in Salemme et al., 2023[50]. Two days after transfection, 50 μM D-Biotin (Thermo Fischer Scientific, Waltham, MA, USA) diluted in the culture medium was added to the cells for 3 h. Cells were washed twice with a biotin-free medium for 1 h, extracted with 500 μl Buffer2 (NaCl 150 mM, TRIS-HCl pH 7.5 20 mM, EDTA 5 mM, Deoxycholate sodium 12 mM), and incubated for 15 min at 4°C. Cell extracts were collected, cropped with a 26G injection needle, sonicated in 4 strokes for 15 sec at 30% amplitude, and centrifuged at 4°C, 15000 g for 15 min. Supernatants were collected and quantified. 500 μg of extracts were incubated overnight with 10 μL of streptavidin-conjugated resin (Pierce™ Streptavidin Agarose; Thermo Fischer Scientific, Waltham, MA, USA). The day after, resins were centrifuged at 4°C, 2500 g, 2 min. Five stepped washes of 1 mL were performed alternating resuspension and centrifugation: one wash in Buffer1 (SDS 2%); two washes in Buffer2 (NaCl 150 mM, TRIS-HCl pH 7.5 20 mM, EDTA 5 mM, Deoxycholate sodium 12 mM); one wash in Buffer3 (NaCl 150 mM, TRIS-HCl pH 7.5 20 mM, EDTA 5 mM, Deoxycholate sodium 12 mM, NP40 1%, SDS 0,01%, Triton X-100 1%); one wash in Buffer4 (NaCl 150 mM, TRIS-HCl pH 7.5 20 mM, EDTA 5mM, Deoxycholate sodium 12 mM, NP40 1%, SDS 0,01%). After the last washing, the resin was dried with a Hamilton needle. Biotinylated proteins were detached from the resin by adding an excess of D-Biotin (1 mM) 1:1 in reduced Sample Buffer (4% SDS) and run on SDS-PAGE.

Neurons cultures transfection

Primary hippocampal neurons isolated from E18.5 embryos were transfected as described in Angelini, Morellato et al., 2022[49]. Alternatively, neurons were magnetofected using NeuroMag Transfection Reagent (OzBiosciences, San Diego, CA, USA): 2 μg of DNA were added in 200 μL of medium, then added to 4 μl of Neuromag magnetic beads, briefly vortexed, and incubated room temperature 15 min. Finally, the solution was added to the neurons, and the cell culture plate was placed on the magnet for 15 minutes.

Immunofluorescence

Neurons at indicated DIV were gently washed with PBS and fixed with ice cold methanol for 10 minutes at -20°C or with 4% PFA 4% sucrose for 10 minutes at room temperature. Fixed neurons were incubated for 30 minutes with blocking solution (PBS, 5% BSA). Primary antibodies were diluted in PBS 1% goat serum and then incubated overnight with fixed neurons in a humid chamber. Alexa Fluor™ secondary antibodies (Thermo Fischer Scientific, Waltham, MA, USA) were incubated for 1 h in the dark. Fixed neurons were mounted on glass slides with Mowiol® 4-88 (Sigma-Aldrich, St. Louis, MO, USA). COS-7 cells were transfected with the indicated constructs. After fixation, transfected cells were blocked with blocking solution (PBS, 5% BSA), incubated with primary antibodies for 1 hour at room temperature and then with Alexa Fluor™ secondary antibodies (Thermo Fischer Scientific, Waltham, MA, USA) for 1 h in the dark. Finally, samples were mounted on glass slides with ProLong™ Gold Antifade Mountant (Thermo Fischer Scientific, Waltham, MA, USA).

Analysis of dendritic spines and fluorescence co-localization

Fluorescence images were acquired using a combined optical video-confocal microscope (ViCo, Nikon Instruments Inc., Melville, NY, USA). Images were digitally captured using a 16-bit camera with Nikon NIS-Elements software (Nikon Instruments Inc., Melville, NY, USA). Cultured neurons and brain slices were imaged with a Leica TCS SP8 confocal system (Leica Microsystems, Wetzlar, DE) equipped with 4 excitation lasers (405 Diode, Argon, DPSS561, HeNe633). Images were acquired with a HCX PL APO 63×/1.4 NA oil-immersion objective on the three coordinates of the space (XYZ planes) with a resolution of 0.09 μm x 0.09 μm x 0.6 μm and were processed and analysed with ImageJ software (Fiji ImageJ software, Rasband, W.S., U.S. National Institutes of Health, Bethesda, MD, USA). Fiji ImageJ software was used to analyse spine density and morphology; colocalization was analysed with JACoP plugin[51].

Small GTPases activity assay

RAC1 activity was assessed by the GST-PAK pull-down assay (RhoA / Rac1 / Cdc42 Activation Assay Combo Biochem Kit; Cyroskeleton, Inc., Denver, CO, USA). RHOA activity was assessed using the Rho Binding Domain (RBD) of the Rho effector protein, Rhotekin. The RBD motif has been shown to bind specifically to the GTP-bound form of RhoA. 20 μg/sample of PAK-GST protein beads or Rhotekin RBD protein beads were used. The assay was performed using 2 mg of crude synaptosomes lysed in ice-cold lysis buffer. The extracts were incubated with PAK-GST beads or Rhotekin RBD beads for 1 h at 4°C under rotation. Beads were then centrifuged at 5200g (4°C) for 1 min, supernatant was discarded, and beads were washed twice in wash buffer (25 mM Tris, pH 7.5, 30 mM $MgCl_2$, 40 mM NaCl). Pellets were resuspended in 25 μL of Laemmli sample buffer in reducing conditions and analyzed by WB.

Mouse perfusion and staining

For the preparation of male P60 littermate WT and *SKT* KO mice in the *Thy1::GFP*+/- background brains, mice were anesthetized with an intraperitoneal injection of a mixture of Zoletil (80 mg/kg; Zolazepam + Tiletamina; Virbac SRL, Milano,IT) and Rompun

(50 mg/g; Xilazina Cloridrato; Elanco Italia SPA, Sesto Fiorentino, IT), transcardially perfused with 20 mL of PBS and then with fixative solution (30 mL of 4% PFA in PBS). After perfusion, brains were dissected and kept in the same fixative solution overnight at 4°C. Brains were sliced into coronary sections of 120 μm using a vibratome and moved in PBS for free-floating immunostaining; following a blocking step in a PBS solution containing 0.05% Triton X-100 and 10% donkey serum (Sigma-Aldrich, St. Louis, MO, USA), sections were incubated overnight at 4°C with the chicken polyclonal antibody against GFP diluted in PBS with 0.05% Triton X-100 and 3% donkey serum. Next, sections were washed three times in PBS and incubated for 1 h at room temperature with the fluorescent secondary antibody anti-Chicken Alexa Fluor™ 488 (Thermo Fischer Scientific, Waltham, MA, USA) at 1:1000 dilution and finally mounted on glass slides. To classify the density and the shape of the dendritic spines we wrote a Python algorithm that has been deposited on Zenodo: https://doi.org/10.5281/zenodo.14230311.

MEA recordings and analysis

Multisite extracellular recordings were performed using the MEA-system as previously described[32,33,52]. Experiments were performed in a non-humidified incubator at 37°C and with 5% CO_2, without replacing the culture medium. Before starting the experiments, cells were allowed to stabilize in the non-humified incubator for 90 seconds; then recordings of the spontaneous activity were carried out for 90 seconds.

Burst analysis was performed using Neuroexplorer software (Nex Technologies, Littleton, MA, USA) after spike sorting operations. A burst consists of a group of spikes with decreasing amplitude[62], thus we set a threshold of at least 3 spikes and a minimum burst duration of 10 ms. We set interval algorithm specifications such as maximum interval to start burst (0.17 sec) and maximum interval to end burst (0.3 sec) recorded in 0.02 sec bins. Burst analysis has been performed by monitoring the following parameters: number of spikes, frequency, number of bursts and burst duration. Cross-correlation probability vs time diagrams were constructed by means of Neuroexplorer software (Nex Technologies, Littleton, MA, USA), using ± 0.5 s and ± 3.5 s and 5 ms bin size. Data are expressed as means ± SEM and statistical significance was calculated by using unpaired t-test. * = $p < 0.05$ were considered significant.

Solutions and drugs for electrophysiology

During the recordings of mEPSCs, the external ACSF solution (119 mM NaCl, 2.5 mM KCl, 1.25 mM NaH_2PO_4, 1.3 mM $MgSO_4$, 2.5 mM $CaCl_2$, 26 mM $NaHCO_3$ and 11 mM Glucose) was supplemented with the D-AP5 (Sigma-Aldrich, St. Louis, MO, USA), picrotoxin (100 μM; Sigma-Aldrich, St. Louis, MO, USA), and CGP 55845 (5 μM; Tocris, Bio-Techne SRL, Milano, IT) to block NMDA, GABAA, and GABAB receptors, respectively. The internal solution contained 120 mM gluconic acid (potassium salt: K-gluconate), 15 mM KCl, 10 mM HEPES, 0.5 mM EGTA, 4 mM Mg-ATP and 0.3 mM Tris-GTP. TTX (300 nM; Tocris, Bio-Techne SRL, Milano, IT) was also added to the external solution to block spontaneous action potentials propagation. For the recordings of eEPSCs, slices were perfused at 1.2 mL/min with ACSF supplemented with D-AP5 (50 μM), picrotoxin (100 μM), and CGP58845 (1 μM) to block NMDA, GABAA, and GABAB receptors, respectively. The internal solution contained 135 mM gluconic acid (potassium salt: K-gluconate), 5 mM NaCl, 2 mM $MgCl_2$, 10 mM HEPES, 0.5 mM EGTA, 2 mM ATP-Tris and 0.4 mM Tris-GTP. We also added QX-314 bromide (10 mM; Tocris, Bio-Techne SRL, Milano, IT) into the internal solution to block postsynaptic Na+ currents activated during recordings.

Patch clamp

Patch electrodes of borosilicate glasses (Hilgenberg, Mansfield, DE) were pulled to a final resistance of 3-6 MΩ. Patch-clamp recordings from CA1 pyramidal neurons were performed in whole-cell configuration using a Multiclamp 700-B amplifier and pClamp 10.0 software (Axon Instruments, Molecular Devices, Sunnyvale, CA, USA)[63]. The miniature excitatory postsynaptic currents (mEPSCs) and evoked EPSCs (eEPSCs) mediated by AMPA-type glutamate receptors were recorded by holding neurons at -70 mV (Vh). The recordings were sampled at 10 kHz using a Digidata 1440A acquisition interface (Molecular Devices, Sunnyvale, CA, USA) and filtered using a low-pass Bessel filter set at 1-2 kHz. Recordings with leak current > 100 pA or series resistance >20 MΩ were discarded. The noise analysis of mEPSCs was performed by using Minianalysis program (Synaptosoft, Leonia, NJ, USA). The amplitude and frequency of mEPSCs was calculated using a peak detector function with threshold amplitude set at 5 pA. The mEPSCs noise analysis was performed considering the parabolic distribution of the variance of current (σ^2) in function of the mEPSCs amplitude[32,35]. All experiments were performed at room temperature in whole cell configuration. Whole-cell recordings of eEPSCs were obtained from CA1 pyramidal neurons which were visualized with an upright microscope. Presynaptic stimuli were delivered through a glass pipette of 1 μm tip diameter filled with ACSF placed in stratum radiatum 200-300 μm away from the recording neuron. Current pulses of 0.1 ms and variable amplitude (100-800 μA) delivered by an isolated pulse stimulator (model 2100; A-M System, Carlsborg, WA, USA) were required to induce monosynaptic eEPSCs with short latency (2-4 ms). The single eEPSCs was recorded every 10 s and analysis was performed with Clampfit software (Axon Instruments, Molecular Devices, Sunnyvale, CA, USA). The paired-pulse facilitation (PPF) was performed by recording the eEPSCs associated with two consecutive pulses separated by interpulse intervals (IEIs) of variable duration (starting from 25 ms and 250 ms) repeated every 10 s. The PPF was calculated as follows: PPF=((A2-A1)/A1)*100 with A1 and A2 indicating the amplitude of the first and second eEPSC, respectively. The size of readily releasable pool (RRP_{syn}) was calculated using the cumulative amplitude analysis[35]. RRP was determined by summing up the eEPSC amplitudes during 40 repetitive stimuli applied at a frequency of 20 Hz for 2 sec. This analysis assumes that the depression during the steady-state phase is limited by a constant recycling of synaptic vesicles and equilibrium occurs between released and recycled synaptic vesicles. The number of data points to include in the linear fitting of the steady-state phase was

evaluated by calculating the best linear fit including the maximal number of data points starting from the last data point, and thus the intercept value with the y-axis makes possible to measure the size of RRPsyn.

Behavioral tests

WT and *SKT* KO males, with an age ranging from 80 to 150 days, from 2 different cohorts, were used for behavioral tests. Mice were housed in a temperature (22 ± 1 °C) and humidity (50 ± 10%) controlled room, in groups of 2-4 per cage, with *ad libitum* access to food and water. Nesting paper material was used for environmental enrichment and diurnal rhythm was maintained with a 12:12 h light–dark cycle (08:00 a.m.–08:00 p.m.). All behavioral experiments were performed during the light cycle between 9 a.m. to 5 p.m. On test day, mice were transported to a dimly illuminated (2 × 40 W, indirect) testing room, adjacent to the animal housing area, and left undisturbed for at least 30 min before testing. At the end of each trial, behavioral tools were accurately cleaned up with ethanol 2% and water. All assays were conducted blindly to mouse genotype.

Activity of daily life

ADL were assessed through nesting and burrowing tests. The tests were performed in home cages, where mice were singularly located and had free access to food and water.

Nest building

Nest-building material (uniformly sized paper strips) was placed in each mouse cage approximately 2 hours before lights-out. The following morning, nest construction was assessed using a scoring system described as follows: 1=paper is untouched; 2=paper is partially torn up; 3=paper is shredded but there is no identifiable nest site; 4=flat nest; 5=perfect nest ranging from 1 (90% of the material remains intact) to 5 (a well-defined three-dimensional nest structure)[38].

Burrowing test

For burrowing, approximately 2.5 hours before the start of the dark cycle a burrowing tube (L: 20 cm; Ø: 7 cm) filled with 200 g of food pellets was placed into the home cage. Two hours later, the remaining material in the tube was weighed. The tube, along with the residual material, was then returned to the cage, and a second measurement of the remaining material was performed the following morning.

Open field test

The OF test was performed to examine locomotor activity and anxious-related behavior. Mice were placed individually in the Phenotyper arena (60 × 60 × 30 cm; Noldus Information Technology, Leesburg, VA, USA) and their behavior was video-tracked for 10 min. Locomotor activity was assessed by measuring the total path-length travelled by the mouse in the arena. Together with the total distance travelled, the time spent in the central zone of the arena was recorded automatically from the digitized image by using a computerized video tracking software (Ethovision XT video track system version 17.5; Noldus Information Technology, Leesburg, VA, USA). Additionally, the time spent in grooming activity was manually recorded by an experimenter blind to the genotype.

Novel object recognition test

The NOR test took place in the same arena where OF was conducted (phase 1, habituation). Mice were then removed from the arena and placed back in its holding cage. After 15 min mice were placed back in the OF arena and allowed to explore two identical objects placed in the two symmetrical corners, opposite the mouse starting point, for 10 min (phase 2, familiarization). After a retention interval of another 15 min (short-term memory), mice were presented to one familiar object (object identical to previous ones) and one novel object (object different to former objects) for another 10 minutes (phase 3, test). Position of the objects was counterbalanced to eliminate bias. After each session, the arena and objects were cleaned with 3% ethanol. The test was video-recorded, and the number and the time of interactions with the objects was manually counted by an experimenter who was blind to the genotype. Exploration of an object was defined as directing the nose at a distance ≤ 2 cm to an object, orientation of an animal's snout toward an object, sniffing or touching with the snout. Discrimination Index (DI) was calculated in the following manner[64]:

$$DI = (\text{Time Exploring Novel Object} - \text{Time Exploring Familiar Object}) / \text{Total Exploration Time}$$

3 mice (2 WT and 1 *SKT* KO) were considered outliers and excluded from the test because the % of time spent in the object exploration was below 0.5% in the test phase and below 1% during the familiarization phase, with a very low number of total object interactions.

Elevated plus maze test

The EPM apparatus consists of a plus-cross shaped (65 × 65 cm) originating from a central platform (5 × 5 cm) elevated 60 cm above the floor. Two opposing arms are enclosed by Plexiglas walls (15 cm, closed arms) and two others are open (open arms). At the start of the trial, the mouse was placed in the center with its nose directed toward an open arm and allowed to freely explore the maze for 10 min. Data was recorded automatically from the digitized image by using a computerized video tracking software (Ethovision XT video track system; Noldus Information Technology, Leesburg, VA, USA).

Rotarod test

WT and *SKT* KO mice were placed on an accelerating rotarod, programmed to increase the initial rotation velocity (4 RPM) of 1 RPM every 8 sec, to a maximum of 40 RPM. The latency of the mice to fall off the rod was recorded over a maximum observation period of 8 min. The average latency before falling was calculated from 2 trials for 2 consecutive days, with a 60 min inter-trial interval.

Barnes maze

Mice were tested in a 15-trials version of the Barnes maze[37]. The maze consisted of a white cleanable disk-shaped arena (140 cm diameter) with 36 holes of 5 cm diameter close to the border and with a comfortable and darkened escape box positioned immediately below the escape hole, in a way to constitute a silent and easily accessible shelter. In the test room, brightly illuminated and with a number of visual cues, a loud white noise (about 70 dB) was played by an external operator through audio speakers placed in the test room. In the habituation phase (trial 1) the mouse was placed underneath a glass beaker and gently guided to the escape hole inducing him to spontaneously enter. During the same day, two more trials were conducted, in which the mice were left free to explore the arena and enter the box, an event that was always coupled to the stop of the white noise and the resting of about one minute in the box. During the acquisition phase (day 2–4), four trials a day were run; the maximum duration of each trial was set to 2 min and the inter-trial interval was about 15 min. The escape latencies (time to enter in the box), the time spent in each quadrant and the total walked distance were recorded. At the end of each trial, the platform and box were cleaned to eliminate possible olfactory cues. For the same reason, the platform was rotated 90 degrees every three trials. On day 6 (probe trial) the escape box was removed, and mice were allowed to freely explore the maze for maximum 2 min. Video recordings were used to evaluate the time elapsed in each of the four quadrants using the Ethovision XT video track system (Noldus Information Technology, Leesburg, VA, USA).

Puzzle Box test

Executive behavior and problem-solving ability were tested in the Puzzle Box[38]. The Puzzle Box contained two compartments of the same size: an illuminated and aversive white start compartment and a black and familiar goal compartment, enriched with the mouse home cage material, such as used sawdust food and paper. The compartments were connected via an open door (HW: 2.5 $\times$ 4 cm) or an underpass (WD: 2 $\times$ 4 cm). In each test trial, the mouse was placed in the start compartment, at the opposite wall to the goal compartment, and the latency to reach the goal compartment was recorded. The total test consisted in 4 different tasks that had to be completed in 10 trials over four days: day 1 – One trial with the door open (task 1), and two trials with the open underpass (task 2). After the task 1, and during all further tasks, the door was always kept closed; day 2 – One repetition of task 2 and two trials with the underpass filled by clean sawdust (task 3) to be removed; day 3 - One repetition of task 3 and two trials with the underpass plugged by a cardboard plug (task 4), to be removed; day 4 – One repetition of task 4. Each day the inter trial interval was 10–15 min. The time limit for trial 1–7 was set to 180 sec; and 240 sec for task 4. The experimenter guided and showed the mice that failed how to get in the goal box. Each mouse was allowed to spend 30 sec in the goal compartment before being returned to the home cage. In task 4 a new, clean cardboard plug was used for each mouse.

Statistics for behavioral tests

Data were recorded in Microsoft Excel (Microsoft Corporation, Redmond, WA, USA) or collected with a computerized video tracking software (Ethovision XT video track system; Noldus Information Technology, Leesburg, VA, USA). For statistical analysis and graph generation, Graphpad Prism v 10.4 (GraphPad Software, San Diego, CA, USA) was used. Significance was set at: * = $p<0.05$, ** = $p<0.01$, *** = $p<0.001$. Normal distribution was tested by Kolmogorov-Smirnov test and significant difference between the 2 groups (WT vs KO) was tested using unpaired t-test for parametric data and by Mann-Whitney test for non-parametric data. For burrowing, two-way ANOVA for repeated measurements with genotype and time as factors was used, followed by uncorrected Fisher's LSD. For Barnes and Puzzle Box, two-way ANOVA for repeated measurements with genotype and time as factors was used, followed by Bonferroni's multiple comparisons test. In the Puzzle Box test, additional Gehan-Breslow-Wilcoxon survival test and Mann-Whitney test for non-parametric data was used to compare genotype performance at each task. In all figures, the number of animals (n) and the number of recorded data points (n) are given as appropriate. In bar graphs, all data points used are pictured together with the mean ± standard error of the mean (SEM).

QUANTIFICATION AND STATISTICAL ANALYSIS

Sample sizes, the number of times the experiment was repeated, and statistical tests are included in the respective figure legends or in the specific result paragraph. All data were analyzed using the appropriate statistical tests as indicated in the respective figure legend. These include One-way ANOVA, Two-way ANOVA, Welch's unpaired t test, paired t test, unpaired t test, Fisher's LSD test, Gehan–Breslow–Wilcoxon survival test, Mann–Whitney test, and Kolmogorov–Smirnov test. Statistical significance was determined as follows *=$p<0.05$, **=$p<0.01$, ***=$p<0.001$, ****=$p<0.0001$, ns=not significative. All statistical analysis was performed with Graphpad Prism v 9.0 or 10.4 (GraphPad Software, San Diego, CA, USA).